Journal of Computational Physics 255 (2013) 53–82

Contents lists available at ScienceDirect

Journal of Computational Physics

www.elsevier.com/locate/jcp

Liquid and liquid–gas flows at all speeds

S. LeMartelot [a], B. Nkonga [b,c], R. Saurel [a,b,d,*]

[a] Polytech'Marseille, Aix-Marseille University, UMR CNRS 7343 IUSTI, 5 rue E. Fermi, 13453 Marseille Cedex 13, France
[b] RS2N, Bastidon de la Caou, 13360 Roquevaire, France
[c] University of Nice, LJAD UMR CNRS 7351, Parc Valrose, 06108 Nice Cedex, France
[d] University Institute of France, 5 rue E. Fermi, 13453 Marseille Cedex 13, France

ARTICLE INFO

Article history:
Received 19 September 2012
Received in revised form 30 July 2013
Accepted 1 August 2013
Available online 12 August 2013

Keywords:
Hyperbolic systems
Multifluid
Multiphase
Venturi
Cavitation
Preconditioning
Unstructured meshes
HLLC

ABSTRACT

All speed flows and in particular low Mach number flow algorithms are addressed for the numerical approximation of the Kapila et al. [1] multiphase flow model. This model is valid for fluid mixtures evolving in mechanical equilibrium but out of temperature equilibrium and is efficient for material interfaces computation separating miscible and non-miscible fluids. In this context, the interface is considered as a numerically diffused zone, captured as well as all present waves (shocks, expansion waves). The same flow model can be used to solve cavitating and boiling flows [2]. Many applications occurring with liquid–gas interfaces and cavitating flows involve a very wide range of Mach number, from 10^{-3} to supersonic (and even hypersonic) conditions with respect to the mixture sound speed. It is thus important to address numerical methods free of restrictions regarding the Mach number.

To do this, a preconditioned Riemann solver is built and embedded into the Godunov explicit scheme. It is shown that this method converges to exact solutions but needs too small time steps to be efficient. An implicit version is then derived, first in one dimension and second in the frame of 2D unstructured meshes. Two-phase flow preconditioning is then addressed in the frame of the Saurel et al. [3] algorithm. Modifications of the preconditioned Riemann solver are needed and detailed. Convergence of both single phase and two-phase numerical solutions are demonstrated with the help of single phase and two-phase steady nozzle flow solutions. Last, the method is illustrated by the computation of real cavitating flows in Venturi nozzles. Vapour pocket size and instability frequencies are reproduced by the model and method without using any adjustable parameter.

1. Introduction

Liquid–gas mixtures and interfacial flows arise in many natural and industrial situations occurring in fluid mechanics, nuclear, environmental and chemical engineering. Many computational approaches consider the two fluids as incompressible (Hirt and Nichols [4], Lafaurie et al. [5], Menard et al. [6] to cite a few). High Mach number flows with material interfaces have also been the subject of important efforts, with various approaches: Front Tracking [7], Level Set and Ghost Fluid [8], diffuse interfaces [9,10,3] and others. Between incompressible and highly compressible fluids, flows with phase change involve both compressible and incompressible effects. An example of boiling liquid–gas flow modelling is given in [11]. In cavitation zones, the liquid–gas mixture is highly compressible as well as the pure gas zones while the pure liquid zones are

* Corresponding author at: Polytech'Marseille, Aix-Marseille University, UMR CNRS 7343 IUSTI, 5 rue E. Fermi, 13453 Marseille Cedex 13, France.
E-mail addresses: sebastien.lemartelot@polytech.univ-mrs.fr (S. LeMartelot), boniface.nkonga@unice.fr (B. Nkonga), richard.saurel@polytech.univ-mrs.fr (R. Saurel).

0021-9991/$ – see front matter
http://dx.doi.org/10.1016/j.jcp.2013.08.001

weakly compressible. In phase change applications gas compressibility is of importance. In cavitating flows, compressibility of all phases is important as the liquid phase change occurs under liquid expansion effects. Moreover, when liquid–gas mixtures appear, the sound propagates with the mixture sound speed [12], which has a non-monotonic behaviour with respect to the volume fraction, resulting in very low sound speed, of the order of a few meters per second. There is thus no difficulty to reach hypersonic flow conditions with liquid–gas mixtures. Consequently, it is important to build numerical methods able to deal with incompressible flows, transonic flows and even hypersonic flows. This issue has been addressed intensively in the context of single phase flows since Harlow and Amsden [13] extending incompressible flow solvers to compressible one and Turkel [14] extending compressible flow solvers to the incompressible limit. Multiphase flows in the low Mach regime has been more addressed by methods issued from incompressible flows [15,16]. However, this poses difficulties when wave dynamics is present, as incompressible flow solvers are not conservative in the compressible flow sense. Also, these methods have difficulties when large density ratios are present. At liquid–gas interfaces, the density ratio may exceed several thousands. Turkel [14] approach, dealing with incompressible flow limit with compressible flow solvers, seems more appropriate. Two-phase cavitating flow models have been addressed in this direction [17,18]. The same kind of approach is considered in the present work. More precisely, we address both liquid–gas interface and cavitating flows with the same theoretical flow model (Kapila et al. [1]) and consider a flow solver close to the preconditioning method of Guillard and Viozat [19]. This approach has some advantages:

- The interfaces are handled routinely, like any point of the flow.
- The dynamic appearance of interfaces (not present initially) is possible thanks to the volume fraction equation structure that allows volume fraction to increase in zones where the velocity divergence is non-zero. This occurs typically in expansion and compression waves and is of major importance in cavitating flows.
- Phase transition can be considered in a thermodynamically consistent way [2].
- The phases mass, mixture momentum and mixture energy are expressed in conservative form, insuring correct wave dynamics in pure fluid zones.
- The addition of surface tension [20] can be done quite easily. In other words, capillary effects are modelled with the help of a capillary tensor and there is no need to resolve the interface structure.

This approach has obviously some drawbacks:

- The interfaces can be excessively diffused, especially when dealing with long time evolutions. But this is exactly the same drawback as contact discontinuity smearing in gas dynamics computations. Efforts to reduce numerical diffusion have been done recently by Kokh and Lagoutière [21], Shukla et al. [22] and So et al. [23].
- Non-conservative equations are present and the numerical approximation of non-conservative terms poses difficulties in the presence of shocks [24,25,3,26,27].
- The building of all Mach number method for this kind of hyperbolic flow model is not an easy task, as it will be shown latter.

As the flow model is conservative regarding the phases mass equations, mixture momentum and mixture energy and since the system is hyperbolic we will adopt a method issued from compressible flow dynamics [14,28,19]. This choice is motivated by the importance of the pressure waves present in many applications, by the presence of huge density ratios at interfaces, that are easier to handle with discontinuity capturing schemes and by the presence of huge Mach number variations. This is mandatory for specific applications, such as:

- liquid–gas flows in nozzles and Venturi tunnels,
- high performance turbo-pumps where cavitation appears,
- propellers,
- water waves breaking,
- flash vapourization.

The key issue when these applications are addressed with the Kapila et al. [1] model is related to the numerical approximation of the flow model in all speed conditions. This issue is addressed in the frame of Turkel, Guillard and Viozat [14,19] formulation.

From a theoretical standpoint, mathematical analysis of the low Mach number limit for classical solutions of the compressible Navier–Stokes has been investigated by many authors (for example, Ebin [29], Klainerman and Majda [30], Schochet [31], Metivier and Schochet [32]). Alazard [33] proved, in a rigorous analysis and general context, the existence of uniformly bounded incompressible limit of the full Navier–Stokes equations. The existence time is there independent of the Mach, the Reynolds and the Peclet numbers and thereby includes the limit for the Euler equation as well. On this theoretical basis, we first consider the single phase Euler equations and derive an approximate preconditioned Riemann solver. When the Godunov scheme is used with this Riemann solver, convergence to the exact nozzle flow solution is obtained. However, the method requires small time steps (much smaller that the conventional CFL restriction) to be stable. We thus consider implicit formulation to overcome this restriction. The HLLC solver of Toro et al. [34] is considered and a Taylor expansion is

done to express its time variation. The method is first presented in the context of the one-dimensional Euler equations and then extended to the one-dimensional Kapila et al. [1] model. After validation against the exact one-dimensional two-phase nozzle flow solution, 2D extension of the algorithm for unstructured meshes is presented. Computational examples are shown in 2D. In particular, a real cavitating flow in 2D Venturi channel is examined. With the help of the new method, very good agreement with the measured cavitation pocket size and detachment frequency is obtained without having recourse to any model or method parameter.

The paper is organized as follows. In Section 2 the Kapila et al. [1] flow model under interest is presented. Its pressure non-equilibrium analogue [3] is presented in the same section as this formulation is more suited to numerical resolution with the approach given in the same reference. In Section 3, the low Mach behaviour of a conventional Godunov type scheme is shown using a single phase nozzle flow solution. In Section 4 the low Mach single phase Riemann solver is presented. It uses the preconditioned Euler equations in the Riemann problem resolution only, while the conventional conservative formulation is used for the solution update. Its extension to the two-phase flow model is then examined. Section 5 deals with time implicit formulation of the preconditioned Godunov method in order to overcome severe stability restrictions. Computational example and validations against experiments are given in Section 6. Conclusions are given in Section 7.

2. Flow model

We consider the two-phase flow model of Kapila et al. [1]. It describes multiphase mixtures evolving in mechanical equilibrium (equal pressures and equal velocities). It is particularly suited to materials interfaces computations, considered as numerical diffusion zones (see for example Saurel et al. [3]). The Kapila et al. [1] model reads:

$$
\begin{aligned}
&\frac{\partial \alpha_1}{\partial t} + \mathbf{u}\cdot\mathbf{grad}(\alpha_1) = K\,\mathrm{div}(\mathbf{u}) \quad \text{where } K = \frac{\rho_2 c_2^2 - \rho_1 c_1^2}{\frac{\rho_1 c_1^2}{\alpha_1} + \frac{\rho_2 c_2^2}{\alpha_2}},\\
&\frac{\partial \alpha_1\rho_1}{\partial t} + \mathrm{div}(\alpha_1\rho_1\mathbf{u}) = 0,\\
&\frac{\partial \alpha_2\rho_2}{\partial t} + \mathrm{div}(\alpha_2\rho_2\mathbf{u}) = 0,\\
&\frac{\partial \rho\mathbf{u}}{\partial t} + \mathrm{div}(\rho\mathbf{u}\otimes\mathbf{u} + P) = 0,\\
&\frac{\partial \rho E}{\partial t} + \mathrm{div}\big((\rho E + P)\mathbf{u}\big) = 0.
\end{aligned}
\tag{1}
$$

c_k represents the sound speed defined by $c_k^2 = \frac{\partial p_k}{\partial \rho_k}\big)_{s_k}$, $k = 1, 2$, P represents the mixture pressure, E represents the mixture total energy, α_k represents the phase volume fraction, ρ_k represents the phase density.

The mixture sound speed is given by the Wood [12] formula and is a consequence of system (1):

$$
\frac{1}{\rho c^2} = \frac{\alpha_1}{\rho_1 c_1^2} + \frac{\alpha_2}{\rho_2 c_2^2}. \tag{2}
$$

In the absence of shocks, system (1) can be complemented by the following entropy equations:

$$
\frac{\partial \alpha_1\rho_1 s_1}{\partial t} + \mathrm{div}(\alpha_1\rho_1 s_1 u) = 0, \qquad \frac{\partial \alpha_2\rho_2 s_2}{\partial t} + \mathrm{div}(\alpha_2\rho_2 s_2 u) = 0. \tag{3}
$$

The thermodynamic closure is achieved with the help of the mixture energy definition,

$$
\rho e = \alpha_1\rho_1 e_1 + \alpha_2\rho_2 e_2
$$

and the pressure equilibrium condition: $p_1 = p_2$.

In the present work, the Stiffened-Gas (SG) EOS is considered for each phase:

$$
p_k = (\gamma_k - 1)\rho_k e_k - \gamma_k P_{\infty,k}. \tag{4}
$$

γ_k and $P_{\infty,k}$ are parameters of the EOS, obtained from reference thermodynamic curves, characteristic of the material and transformation under study. See Le Métayer et al. [35] for details.

In the context of fluids governed by SG EOS (4), the mixture EOS reads:

$$
P = \frac{\rho e - \left(\frac{\alpha_1\gamma_1 P_{\infty,1}}{\gamma_1 - 1} + \frac{\alpha_2\gamma_2 P_{\infty,2}}{\gamma_2 - 1}\right)}{\frac{\alpha_1}{\gamma_1 - 1} + \frac{\alpha_2}{\gamma_2 - 1}}. \tag{5}
$$

Obviously, other convex EOS can be considered instead of (4) for the building of (5). The numerical approximation of the Kapila et al. [1] model is addressed in the frame of Godunov type finite volume schemes. To overcome the difficulties

related to the approximation of the non-conservative term $K\,\mathrm{div}(u)$ in the volume fraction equation of system (1) a pressure non-equilibrium system (6) is considered during the transport step and a proper projection is achieved to recover the target model (1). The pressure non-equilibrium system reads:

$$\begin{aligned}
&\frac{\partial \alpha_1}{\partial t} + \mathbf{u}\cdot\mathbf{grad}(\alpha_1) = \mu(p_1 - p_2),\\
&\frac{\partial \alpha_1\rho_1}{\partial t} + \mathrm{div}(\alpha_1\rho_1\mathbf{u}) = 0,\\
&\frac{\partial \alpha_2\rho_2}{\partial t} + \mathrm{div}(\alpha_2\rho_2\mathbf{u}) = 0,\\
&\frac{\partial \alpha_1\rho_1 e_1}{\partial t} + \mathrm{div}(\alpha_1\rho_1 e_1\mathbf{u}) + \alpha_1 p_1\,\mathrm{div}(\mathbf{u}) = -p_I\mu(p_1 - p_2),\\
&\frac{\partial \alpha_2\rho_2 e_2}{\partial t} + \mathrm{div}(\alpha_2\rho_2 e_2\mathbf{u}) + \alpha_2 p_2\,\mathrm{div}(\mathbf{u}) = p_I\mu(p_1 - p_2),\\
&\frac{\partial \rho\mathbf{u}}{\partial t} + \mathrm{div}(\rho\mathbf{u}\otimes\mathbf{u} + P) = 0,\\
&\frac{\partial \rho E}{\partial t} + \mathrm{div}\big((\rho E + P)\mathbf{u}\big) = 0
\end{aligned} \tag{6}$$

where μ represents the pressure relaxation coefficient, p_I represents the interfacial pressure defined by $p_I = \frac{Z_1 p_2 + Z_2 p_1}{Z_1 + Z_2}$, with $Z_k = \rho_k c_k$, the phase k acoustic impedance. e_k and p_k represent the phase k internal energy and pressure respectively.

It is important to note that in this system the internal energies of each phase are independent variables and their evolution is described by two additional equations. The mixture pressure is now related to the phases' internal energies:

$$P = \alpha_1 p_1 + \alpha_2 p_2 \tag{7}$$

where $p_1 = p_1(\rho_1, e_1)$ and $p_2 = p_2(\rho_2, e_2)$.

The non-equilibrium system (6) is hyperbolic and appropriate to overcome the difficulties related to the discretization of the volume fraction equation, in particular regarding positivity issues. System (6) is used to reach solutions of system (1) in the limit of infinite pressure relaxation, i.e. when μ tends to infinity.

It is worth to mention that system (6) is overdetermined. Indeed, the total energy equation is a consequence of the phases energy equations and the mixture momentum one. This over-determination will be used to correct the inaccuracies appearing during the numerical integration of $\alpha_k p_k\,\mathrm{div}(\mathbf{u})$, the non-conservative terms of the internal energy equations [3]. Overdetermined systems have already been considered for numerical approximation issues in different contexts by Babii et al. [36] for example.

Let us mention that this formulation is needed not only when two-phase shock waves are present, but also when cavitation is considered, as in the present paper. Indeed, when cavitation comes from geometrical effects, closed to walls, a normal velocity discontinuity appears. Indeed, wall boundary conditions are solved with the help of a mirror state, resulting in unbounded velocity divergence and undefined non-conservative product in the volume fraction equation of system (1). It means that the building of a positive scheme based on system (1) in realistic cavitating flow conditions is an issue. Formulation (6) overcomes this difficulty. Also, many practical situations of cavitating flow involve huge Mach number variations, and robustness of the algorithm is mandatory. Formulation (6) is particularly robust. The algorithm based on the overdetermined formulation (6) can be summarized as follows. System (6) is rearranged as follows:

$$\frac{\partial \boldsymbol{U}}{\partial t} + \mathrm{div}\big(\boldsymbol{F}(\boldsymbol{U})\big) + \boldsymbol{H}(\boldsymbol{U})\,\mathrm{div}(\mathbf{u}) = \mu(p_1 - p_2)\boldsymbol{S}(\boldsymbol{U}) \tag{8}$$

where,

$$\boldsymbol{U} = \begin{pmatrix} \alpha_1 \\ \alpha_1\rho_1 \\ \alpha_1\rho_2 \\ \rho\mathbf{u} \\ \rho E \\ \alpha_1\rho_1 e_1 \\ \alpha_2\rho_2 e_2 \end{pmatrix}, \quad \boldsymbol{F}(\boldsymbol{U}) = \begin{pmatrix} \alpha_1\mathbf{u} \\ \alpha_1\rho_1\mathbf{u} \\ \alpha_1\rho_2\mathbf{u} \\ \rho\mathbf{u}\otimes\mathbf{u} + P \\ (\rho E + P)\mathbf{u} \\ \alpha_1\rho_1 e_1\mathbf{u} \\ \alpha_2\rho_2 e_2\mathbf{u} \end{pmatrix}, \quad \boldsymbol{H}(\boldsymbol{U}) = \begin{pmatrix} -\alpha_1 \\ 0 \\ 0 \\ 0 \\ 0 \\ \alpha_1 p_1 \\ \alpha_2 p_2 \end{pmatrix} \quad \text{and} \quad \boldsymbol{S}(\boldsymbol{U}) = \begin{pmatrix} 1 \\ 0 \\ 0 \\ 0 \\ 0 \\ -p_I \\ p_I \end{pmatrix}. \tag{9}$$

Each integration time step is structured as follows [3]:

Initialization: At a given time step, the flow is in mechanical equilibrium, in particular in pressure equilibrium. The set of variables is given by:

$$\boldsymbol{U}^n \equiv \boldsymbol{U}\big(\boldsymbol{V}^n\big) \quad \text{with } \boldsymbol{V}^n = \big(\alpha_1^n, \rho_1^n, \rho_2^n, u^n, e_1^n\big(\rho_1^n, P^n\big), e_2^n\big(\rho_2^n, P^n\big), E^n\big)^T.$$

Fig. 1. Nozzle connected to a tank at the inlet and to a prescribed pressure at the outlet.

Non-equilibrium evolution: The pressure relaxation terms are removed ($\mu = 0$) and the hyperbolic pressure non-equilibrium system is solved. At the end of this evolution step a temporary flow state is determined:

$$\frac{\partial \boldsymbol{U}}{\partial t} + \operatorname{div}\big(\boldsymbol{F}(\boldsymbol{U})\big) + \boldsymbol{H}(\boldsymbol{U})\operatorname{div}(\mathbf{u}) = 0 \quad \mapsto \quad \widetilde{\boldsymbol{U}}^{n+1} \equiv \boldsymbol{U}\big(\widetilde{\boldsymbol{V}}^{n+1}\big)$$
$$\text{with } \widetilde{\boldsymbol{V}}^{n+1} = \big(\tilde{\alpha}_1^{n+1}, \tilde{\rho}_1^{n+1}, \tilde{\rho}_2^{n+1}, u^{n+1}, \tilde{e}_1^{n+1}, \tilde{e}_2^{n+1}, E^{n+1}\big). \tag{10}$$

Projection to pressure equilibrium: This step deals with the projection of the previous pressure non-equilibrium state onto a pressure equilibrium one:

$$\frac{\partial \boldsymbol{U}}{\partial t} = \mu(p_1 - p_2)\boldsymbol{S}(\boldsymbol{U}) \quad \mapsto \quad \boldsymbol{U}^{n+1} \equiv \boldsymbol{U}\big(\boldsymbol{V}^{n+1}\big)$$
$$\text{with } \boldsymbol{V}^{n+1} = \big(\alpha_1^{n+1}, \rho_1^{n+1}, \rho_2^{n+1}, u^{n+1}, e_1^{n+1}\big(\rho_1^{n+1}, P^{n+1}\big), e_2^{n+1}\big(\rho_2^{n+1}, P^{n+1}\big), E^{n+1}\big).$$

This is done by determining the asymptotic solution of the remaining relaxation ODE system in the limit $\mu \to +\infty$. The asymptotic state is determined by the resolution of a non-linear algebraic equation. Details may be found, for example, in [3]. In particular, it is shown in Appendix B of this reference, that this strategy results in approximating solutions of (1).

It is worth to mention that:

- The equilibrium pressure p^{n+1} is determined from the mixture EOS (5), based on the mixture total energy E^{n+1}, for which there is no conservation issue.
- Both steps in this strategy preserve volume fraction positivity.
- Both steps preserve phases' mass conservation, mixture momentum and energy conservation.
- The entropy inequality is also preserved during each step.

This algorithm has shown robustness, accuracy and versatility for various flow models ranging from interfaces, supercavitating flows [2], detonation waves [37], powder compaction [38], solid–fluid coupling [39] in severe high speed conditions. We address here arbitrary velocity flow conditions and particularly low Mach number conditions.

3. Low Mach behaviour of conventional Godunov type schemes

To illustrate the fundamental difficulties of low Mach number computations, we consider a basic situation of 1D nozzle flow. We first examine the behaviour of the Godunov method in this limit for single phase liquid flows. We consider the nozzle geometry given in Fig. 1 connected to an inlet imposed mass flow rate m_0 and imposed stagnation enthalpy H_0 and to a prescribed outlet pressure, p_{out}. The first-order Godunov method with HLLC approximate Riemann solver is used to compute the smooth varying nozzle flow. Details are given in Appendix A. Computations to steady state are achieved with uniform meshes of different sizes. The exact quasi-1D solution is computed using the method described in [40].

All computations are achieved with a time step satisfying CFL = 0.5. The outlet pressure boundary condition and the inlet stagnation enthalpy and mass flow rate are solved by the method of Osher and Chakravarthy [41]. The geometrical data and boundary conditions for the liquid flow are:

- Inlet cross section: 0.14657 m^2.
- Throat cross section: 0.06406 m^2.
- Outlet cross section: 0.14657 m^2.

The nozzle profile is piecewise linear with respect to the surface area. The nozzle length is 1 m while the throat is located 0.5 m from the inlet. The boundary conditions are given by:

$$\begin{cases} m_0 = 7000\ \mathrm{kg\,m^{-2}\,s^{-1}}, \quad H_0 = \dfrac{P_0 + \gamma P_\infty}{(\gamma - 1)\rho_0} + \dfrac{P_0}{\rho_0} + \dfrac{m_0^2}{2\rho_0} \\ \quad \text{with } P_0 = 0.1\ \mathrm{MPa},\ \rho_0 = 1000\ \mathrm{kg\,m^{-3}},\ \gamma = 4.4,\ P_\infty = 600\ \mathrm{MPa}. \end{cases}$$

The exact and computed velocity and pressure profiles are shown in Fig. 3 for various mesh sizes: 100, 1000 and 10 000 cells.

The computed and exact velocity profiles are in excellent agreement but the pressure and density fields present large errors. Regarding the pressure field, the jump at throat is not a computational artefact due to a lack of "well balance" effect in the Riemann solver, boundary conditions or slope singularity at throat. The 500% error is strictly due to density fluctuations combined with the SG EOS (4) stiffness. Mesh refinement analysis illustrates the convergence issue, that is clearly not a consistence one. Quasi-convergent results are obtained with 10 000 cells (Fig. 2). Table 1 shows computational

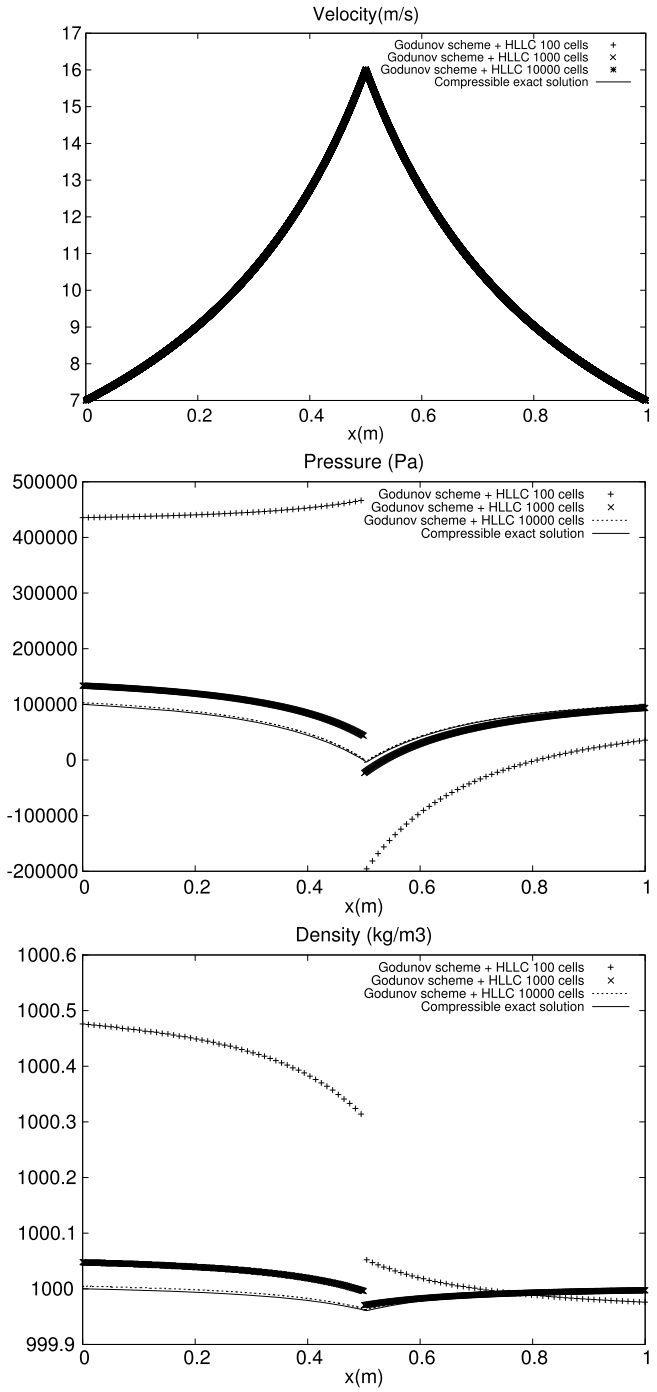

Fig. 2. Computed velocity, pressure and density profiles in the Laval liquid nozzle flow with 100, 1000 and 10 000 cells against the compressible exact solution. The Godunov scheme solutions present severe fluctuations. The error decreases under mesh refinement.

Table 1
Computational time versus mesh size for the 1D liquid nozzle flow test.

Mesh size	Calculation time
100 cells	20 s
1000 cells	33 min 56 s
10 000 cells	59 h 16 min 48 s

times to reach steady state inside the piecewise linear nozzle versus mesh size. It is clear that the method is extremely expensive, even for 1D computations.

4. Improving numerical convergence at low Mach number limit

As single phase computations have shown serious issues under low Mach number conditions (Fig. 2), it is clear that efforts have to be done to improve the asymptotic behaviour of Godunov type schemes at low Mach. This has to be done prior to consider numerical approximation of the two-phase flow model (1). We thus address the numerical approximation of the Euler equation first. The two-phase flow model (1) will be addressed in a second part. For the sake of simplicity, the analysis is carried out in 1D, multi-D extension being addressed later.

4.1. Low Mach number preconditioning

As shown previously, the conventional Godunov method converges to the exact solution under low Mach conditions if very fine resolution is used. Such meshes being impracticable for multi-dimensional applications, modifications have to be done. We are seeking a numerical method valid for all speeds flows, from transonic to low Mach number. In this area, Turkel [14] established a preconditioning method to guarantee convergence of the results at steady state. Unsteady extensions have been done with several approaches. Choi and Merkle [28] introduced an approach with two time steps, an artificial one and a physical one. An analysis of various compressible flow approaches for unsteady flows is given in [42]. Recent extension to discontinuous Galerkin methods is given in [43]. Moreover, extension of dual time stepping methods to cavitating two-phase flows has been addressed by several authors [17,18,44]. Another approach was derived by Guillard and Viozat [19] where only the flux numerical dissipation was modified to reach convergence in both low and high Mach number conditions. This approach is considered in the present work as it guarantees conservation and convergence even when discontinuities such as shock waves are present. Indeed, the conservative formulation of the equations as well as the equation of state are unmodified. This results in unchanged jump conditions across the various waves and correct wave speed computation.

This strategy is presented hereafter in the context of the Euler equations. The HLLC Riemann solver of Toro et al. [34] is considered and wave speeds for all Mach number flow situations are estimated following Murrone and Guillard [45] and Braconnier and Nkonga [46] with the help of the following analysis. For the approximate Riemann problem resolution only (not for the solution update), the Euler equations are considered under primitive variables formulation:

$$\begin{aligned}
&\frac{\partial \rho}{\partial t} + \rho \frac{\partial u}{\partial x} + u \frac{\partial \rho}{\partial x} = 0,\\
&\frac{\partial u}{\partial t} + u \frac{\partial u}{\partial x} + \frac{1}{\rho} \frac{\partial p}{\partial x} = 0,\\
&\frac{\partial p}{\partial t} + u \frac{\partial p}{\partial x} + \rho c^2 \frac{\partial u}{\partial x} = 0.
\end{aligned} \tag{11}$$

4.1.1. Dimensionless variables

These equations are expressed in dimensionless variables with the help of the following definitions: $\rho = [\rho]\tilde{\rho}$, $u = [u]\tilde{u}$, $p = [p]\tilde{p}$, $x = [x]\tilde{x}$ and $t = [t]\tilde{t}$, where $[f]$ represents a characteristic scale of the corresponding variable and $\tilde{f}$ the dimensionless one. System (11) becomes:

$$\begin{aligned}
&\frac{\partial \tilde{\rho}}{\partial \tilde{t}} + \tilde{\rho} \frac{\partial \tilde{u}}{\partial \tilde{x}} + \tilde{u} \frac{\partial \tilde{\rho}}{\partial \tilde{x}} = 0,\\
&\frac{\partial \tilde{u}}{\partial \tilde{t}} + \tilde{u} \frac{\partial \tilde{u}}{\partial \tilde{x}} + \frac{[p]}{[\rho][u]^2 \tilde{\rho}} \frac{\partial \tilde{p}}{\partial \tilde{x}} = 0,\\
&\frac{\partial \tilde{p}}{\partial \tilde{t}} + \tilde{u} \frac{\partial \tilde{p}}{\partial \tilde{x}} + \frac{[\rho][c]^2}{[p]} \tilde{\rho} \tilde{c}^2 \frac{\partial \tilde{u}}{\partial \tilde{x}} = 0.
\end{aligned} \tag{12}$$

A pressure scaling has to be defined. At least, three options are possible:

- An 'acoustic' scaling, corresponding to,

$$[p] = [\rho][c][u]. \tag{13}$$

- A 'dynamic pressure' scaling, corresponding to,

$$[p] = [\rho][u]^2. \tag{14}$$

- A 'bulk modulus' scaling, corresponding to,

$$[p] = [\rho][c]^2. \tag{15}$$

The first two scalings lead to wrong wave speed propagation and are, consequently, rejected. Indeed, it is not possible to recover an admissible entropy equation from the mass and pressure equations. Should, otherwise, the equation of state be changed. Choosing the last one results in the following system:

$$\begin{aligned}
&\frac{\partial \tilde{\rho}}{\partial \tilde{t}} + \tilde{\rho}\frac{\partial \tilde{u}}{\partial \tilde{x}} + \tilde{u}\frac{\partial \tilde{\rho}}{\partial \tilde{x}} = 0,\\
&\frac{\partial \tilde{u}}{\partial \tilde{t}} + \tilde{u}\frac{\partial \tilde{u}}{\partial \tilde{x}} + \frac{1}{M^2\tilde{\rho}}\frac{\partial \tilde{p}}{\partial \tilde{x}} = 0,\\
&\frac{\partial \tilde{p}}{\partial \tilde{t}} + \tilde{u}\frac{\partial \tilde{p}}{\partial \tilde{x}} + \tilde{\rho}\tilde{c}^2\frac{\partial \tilde{u}}{\partial \tilde{x}} = 0.
\end{aligned} \tag{16}$$

As shown in the next subsection, the 'bulk modulus' scaling formally admits the incompressible Euler equations as asymptotic limit when the Mach number tends to zero. We thus consider system (16) in the following where the symbol $\tilde{}$ is dropped for the sake of simplicity.

4.1.2. Asymptotic analysis

We now examine the limit system associated to system (16) when the Mach number tends to zero. The various flow variables 'f' are expanded as:

$$f = f_0 + \epsilon f_1 + \epsilon^2 f_2, \quad \text{where } \epsilon \to 0^+.$$

At the order ϵ^{-2} system (16) implies,

$$\frac{\partial p_0}{\partial x} = 0. \tag{17}$$

At the order ϵ^{-1} it implies,

$$\frac{\partial p_1}{\partial x} = 0, \tag{18}$$

and at leading order the limit system reads:

$$\begin{aligned}
&\frac{\partial \rho_0}{\partial t} + u_0\frac{\partial \rho_0}{\partial x} + \rho_0\frac{\partial u_0}{\partial x} = 0,\\
&\frac{\partial u_0}{\partial t} + u_0\frac{\partial u_0}{\partial x} + \frac{1}{\rho_0}\frac{\partial p_2}{\partial x} = 0,\\
&\frac{\partial p_0}{\partial t} + \rho_0 c_0^2\frac{\partial u_0}{\partial x} = 0.
\end{aligned} \tag{19}$$

Under the condition,

$$\frac{\partial p_0}{\partial t} = 0, \tag{20}$$

system (19) tends formally to the incompressible Euler equations,

$$\begin{aligned}
&\rho_0 = const,\\
&\frac{\partial u_0}{\partial x} = 0,\\
&\frac{\partial u_0}{\partial t} + u_0\frac{\partial u_0}{\partial x} + \frac{1}{\rho_0}\frac{\partial p_2}{\partial x} = 0.
\end{aligned} \tag{21}$$

To enforce condition (20), an extra coefficient is added to the pressure equation of system (19):

$$\frac{1}{M^2}\frac{\partial p_0}{\partial t} + \rho_0 c_0^2\frac{\partial u_0}{\partial x} = 0. \tag{22}$$

This penalization strategy, due to Turkel [14], forces solutions of system (19) to converge to incompressible solutions of system (21).

4.1.3. System considered for the Riemann problem solution

Inserting (22) in (19) and using (17)–(18), the following leading order system is obtained:

$$\begin{aligned}
&\frac{\partial \rho}{\partial t} + u\frac{\partial \rho}{\partial x} + \rho\frac{\partial u}{\partial x} = 0,\\
&\frac{\partial u}{\partial t} + u\frac{\partial u}{\partial x} + \frac{1}{\rho}\frac{\partial p}{\partial x} = 0,\\
&\frac{\partial p}{\partial t} + M^2 u\frac{\partial p}{\partial x} + M^2\rho c^2\frac{\partial u}{\partial x} = 0.
\end{aligned} \tag{23}$$

This system is hyperbolic and has the following wave speeds: u, $u+\tilde{c}_+$, $u-\tilde{c}_-$, with,

$$\tilde{c}_- = \frac{(1-M^2)u + \sqrt{(M^2-1)^2u^2 + 4M^2c^2}}{2}, \qquad \tilde{c}_+ = \frac{(M^2-1)u + \sqrt{(M^2-1)^2u^2 + 4M^2c^2}}{2}. \tag{24}$$

These wave speeds are directly used in the HLLC solver (64). It is worth to mention that the Euler system is modified in the Riemann problem resolution only, where formulation (23) is used. With the fluxes computed with the HLLC solver, the Godunov method (63) is used with the conventional conservative formulation of the Euler equations and unmodified equation of state. Thus, the solved flow model corresponds exactly to the Euler equations with the EOS (4). In this variant of the Turkel [14] method, due to Guillard and Viozat [19], the preconditioning only appears in the flux computation. The formulation remains conservative and guarantees correct jumps across waves, as will be illustrated later. It only acts on the numerical dissipation. As the conservative formulation is used, even strong discontinuities can be handled by the method. Also, as the Mach number can be varied in (23), the method is able to compute fast flows. This remarkable feature is due to Guillard and Viozat [19]. The validity and efficiency of this method is illustrated later. We now address an extension to the two-phase flow model (1) and its pressure non-equilibrium variant (6).

4.1.4. Two-phase low Mach preconditioning

The pressure non-equilibrium model (6) in primitive variables formulation reads:

$$\begin{aligned}
&\frac{\partial \alpha_1}{\partial t} + u\frac{\partial \alpha_1}{\partial x} = 0,\\
&\frac{\partial \alpha_1\rho_1}{\partial t} + \alpha_1\rho_1\frac{\partial u}{\partial x} + u\frac{\partial \alpha_1\rho_1}{\partial x} = 0,\\
&\frac{\partial \alpha_2\rho_2}{\partial t} + \alpha_2\rho_2\frac{\partial u}{\partial x} + u\frac{\partial \alpha_2\rho_2}{\partial x} = 0,\\
&\frac{\partial u}{\partial t} + u\frac{\partial u}{\partial x} + \frac{1}{\rho}\frac{\partial P}{\partial x} = 0,\\
&\frac{\partial e_1}{\partial t} + u\frac{\partial e_1}{\partial x} + \frac{p_1}{\rho_1}\frac{\partial u}{\partial x} = 0,\\
&\frac{\partial e_2}{\partial t} + u\frac{\partial e_2}{\partial x} + \frac{p_2}{\rho_2}\frac{\partial u}{\partial x} = 0,\\
&\frac{\partial P}{\partial t} + u\frac{\partial P}{\partial x} + \rho c^2\frac{\partial u}{\partial x} = 0
\end{aligned} \tag{25}$$

where $P = \alpha_1 p_1 + \alpha_2 p_2$.

The pressure relaxation terms have been omitted as they are solved separately. This system admits the following frozen sound speed defined by:

$$c_f = \sqrt{Y_1 c_1^2 + Y_2 c_2^2}. \tag{26}$$

This sound speed is very different from the mechanical equilibrium one given by (2). However, the equilibrium sound speed is recovered after the projection to pressure equilibrium, as summarized in Section 2. Theoretical details on sound propagation in media with relaxation may be found, for example, in [47]. In the present two-phase flow context, the sound speed has dramatic variations, from formula (26) to (2). Theoretical proof is given in [1] or [3].

As system (6) is overdetermined (see again Section 2 for details), its primitive formulation is also overdetermined. In particular, the mixture pressure equation and the two internal energy equations form an overdetermined subsystem.

During low Mach preconditioning, in order to force the incompressibility condition,

$$\frac{\partial u}{\partial x} = 0, \tag{27}$$

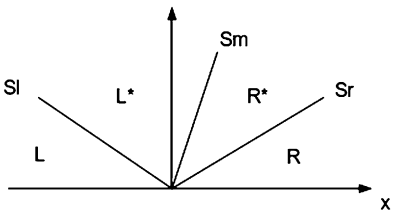

Fig. 3. Schematics representation of the Riemann problem and associated wave speeds.

when the Mach number tends to zero, the pressure equation has been modified with a penalization coefficient (Eq. (22)), resulting in system (23) in the single phase flows context. Here, the same preconditioned pressure formulation is adopted:

$$\frac{1}{M^2}\frac{\partial P}{\partial t} + u\frac{\partial P}{\partial x} + \rho c^2 \frac{\partial u}{\partial x} = 0. \tag{28}$$

Modifying the mixture pressure equation immediately modifies the wave speeds, as previously in the single phase flow case:

$$\tilde{c}_- = \frac{(1-M^2)u + \sqrt{(M^2-1)^2u^2 + 4M^2c_f^2}}{2}, \qquad \tilde{c}_+ = \frac{(M^2-1)u + \sqrt{(M^2-1)^2u^2 + 4M^2c_f^2}}{2}. \tag{29}$$

These two formulas are identical to those given by Murrone and Guillard [45] and Braconnier and Nkonga [46]. However, the Mach number is calculated with the sound speed (26). With the help of (27), the incompressible limit of system (25) becomes:

$$\begin{aligned}
&\frac{\partial \alpha_1}{\partial t} + u\frac{\partial \alpha_1}{\partial x} = 0,\\
&\frac{\partial \rho_1}{\partial t} + u\frac{\partial \rho_1}{\partial x} = 0,\\
&\frac{\partial \rho_2}{\partial t} + u\frac{\partial \rho_2}{\partial x} = 0,\\
&\frac{\partial u}{\partial t} + u\frac{\partial u}{\partial x} + \frac{1}{\rho}\frac{\partial P}{\partial x} = 0,\\
&\frac{\partial p_1}{\partial t} + u\frac{\partial p_1}{\partial x} = 0 \quad \text{or alternatively} \quad \frac{\partial e_1}{\partial t} + u\frac{\partial e_1}{\partial x} = 0,\\
&\frac{\partial p_2}{\partial t} + u\frac{\partial p_2}{\partial x} = 0 \quad \text{or alternatively} \quad \frac{\partial e_2}{\partial t} + u\frac{\partial e_2}{\partial x} = 0,\\
&\frac{\partial u}{\partial x} = 0.
\end{aligned} \tag{30}$$

The limit internal energy equations will be of particular help to determine appropriate jump relations for the low Mach Riemann solver presented hereafter.

Solving the Riemann problem. Using the notations given in Fig. 3, the various wave speeds are given by:

$$Sl = u_l - \tilde{c}_l, \qquad Sr = u_r + \tilde{c}_r, \quad \text{with definition (29)}, \tag{31}$$

and

$$S_M = \frac{S_R(\rho u)_R - S_L(\rho u)_L - ((\rho u^2 + p)_R - (\rho u^2 + p)_L)}{S_R\rho_R - S_L\rho_L - ((\rho u)_R - (\rho u)_L)}. \tag{32}$$

The two-phase Riemann problem is solved as detailed in [3], except for the internal energy equations.
The U_L^* and U_R^* states are determined with the following relations:

$$(\alpha_k\rho_k)_R^* = (\alpha_k\rho_k)_R\frac{S_R - u_R}{S_R - S_M}, \tag{33}$$

$$(\alpha_k\rho_k)_L^* = (\alpha_k\rho_k)_L\frac{S_L - u_L}{S_L - S_M}, \tag{34}$$

$$p^* = p_R + \rho_R u_R(u_R - S_R) - \rho_R^* S_M(S_M - S_R), \quad \text{where } \rho_R^* = \sum_k (\alpha_k\rho_k)_R^*, \tag{35}$$

$$E_R^* = \frac{\rho_R E_R (u_R - S_R) + p_R u_R - p^* S_M}{\rho_R^* (S_M - S_R)}, \tag{36}$$

$$E_L^* = \frac{\rho_L E_L (u_L - S_L) + p_L u_L - p^* S_M}{\rho_L^* (S_M - S_L)}. \tag{37}$$

In the absence of relaxation effects, the volume fraction is constant along fluid trajectories:

$$\alpha_{k,R}^* = \alpha_{k,R}, \qquad \alpha_{k,L}^* = \alpha_{k,L}. \tag{38}$$

Once U_L^* and U_R^* are determined, the solution flux vector, F^*, is computed using relation (64) and the following definitions:

$$U = \begin{pmatrix} \alpha_1 \\ \alpha_1\rho_1 \\ \alpha_2\rho_2 \\ \alpha_1\rho_1 e_1 \\ \alpha_2\rho_2 e_2 \\ \rho u \\ \rho E \end{pmatrix}, \qquad F = \begin{pmatrix} \alpha_1 u \\ \alpha_1\rho_1 u \\ \alpha_2\rho_2 u \\ \alpha_1\rho_1 e_1 u \\ \alpha_2\rho_2 e_2 u \\ \rho u^2 + P \\ (\rho E + P)u \end{pmatrix}. \tag{39}$$

In the low Mach number limit, the internal energy equations reduce to:

$$\begin{aligned} &\frac{\partial e_1}{\partial t} + u\frac{\partial e_1}{\partial x} = 0, \\ &\frac{\partial e_2}{\partial t} + u\frac{\partial e_2}{\partial x} = 0. \end{aligned} \tag{40}$$

Therefore, there is no internal energy jump through the Sl and Sr waves. Thus, the internal energies in the L^* and R^* states are computed as follows:

$$\begin{aligned} &e_{k,L}^* = e_{k,L}, \\ &e_{k,R}^* = e_{k,R}. \end{aligned} \tag{41}$$

These two last relations are very different from the isentropes used in Murrone and Guillard [45]. Let us also mention that Eqs. (40) correspond to the asymptotic limit of the entropy equations of system (25) and that they also correspond to the same limit of the entropy equations (3) corresponding to the mechanical equilibrium system. The influence of the jump relations (41) will be examined later with computational experiments.

4.2. Preconditioned Riemann solvers illustrations

4.2.1. Single phase nozzle flow

The explicit Godunov scheme of Appendix A with HLLC Riemann solver is used, with the preconditioned wave speed (24) derived previously.

In the formulation (23), and consequently in the associated Riemann solver given in Appendix A, the Mach number M is set to a reference value M_{ref} which is either used as a constant in the entire flow field or considered variable at each cell boundary. To illustrate the method efficiency, the same nozzle flow problem as studied previously in Fig. 2 is considered.

A coarse mesh with 100 grid points is considered and the M_{ref} influence is studied. Corresponding results are shown in Fig. 4 at steady state.

On this test case, the unpreconditioned Godunov method predicts negative pressure inside the nozzle divergent, which is possible in the frame of SG EOS. Preconditioning the method corrects this defect. These results clearly show the benefit of the Riemann solver preconditioning as close agreement with the exact solution is reached. However, the explicit scheme is not efficient enough for practical applications because of the stability restriction (44), due to [48]. An implicit formulation will be addressed later to overcome this restriction. Before addressing this extension, the explicit formulation is examined (for obvious simplicity reasons) in the two-phase flow context.

4.2.2. Two-phase nozzle flow

To illustrate the two-phase low Mach number preconditioning, the same nozzle flow problem as studied previously is considered. However, the liquid water at the inflow now contains a small fraction of air.

Mass flow rate and total enthalpy are imposed at left while the right outlet is opened to the atmosphere. The fluids used in the calculations correspond to liquid water and air, with the following SG EOS (4) parameters $\gamma_{water} = 4.4$, $P_{\infty,water} = 600$ MPa, $\gamma_{air} = 1.4$, $P_{\infty,air} = 0$ Pa. The imposed conditions at left inflow are the following:

$$m = 6500\ \mathrm{kg\,m^{-2}\,s^{-1}}, \qquad \rho_{water} = 1000\ \mathrm{kg\,m^{-3}}, \qquad \rho_{air} = 1\ \mathrm{kg\,m^{-3}}, \qquad \alpha_{water,0} = 0.9999, \qquad P = 0.1\ \mathrm{MPa}.$$

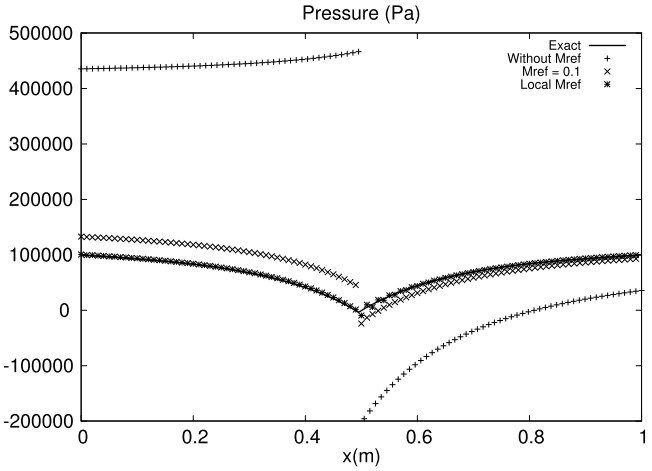

Fig. 4. Computed pressure profiles in the Laval liquid nozzle flow test with $M_{ref} = 0.1$, $M_{ref} =$ local Mach number and without M_{ref} are compared against the compressible exact solution. The error decreases dramatically as soon as M_{ref} is used and tends to the local Mach number.

The imposed total enthalpy is computed with $\rho_{water}, \rho_{air}, \alpha_{water,0}$ and P. With these boundary conditions, the numerical solution has been computed using different values of $M_{ref,min}$: 0.1, 0.05, 0.01 and two meshes containing 100 cells and 200 cells, respectively. $M_{ref,min}$ will be defined in the next subsection. The quasi-1D two-phase reference solution is computed using the method described in Appendix B. Fig. 5 shows clearly that the waves' speed choice and modification of the solver have dramatic consequences on method convergence in the low Mach number limit. These results are compared to the ones obtained with Murrone and Guillard [45] low Mach preconditioning technique in Fig. 6. These results show that, even though the Murrone and Guillard [45] low Mach preconditioning technique improve solution accuracy, convergence to the exact solution is not reached at all. This is mainly a consequence of inappropriate energy jump conditions used in the Riemann solver by these authors in the low Mach limit. Murrone and Guillard method uses isentropic evolutions across the left and right facing waves whereas relations (41) are used herein.

4.2.3. Preconditioning method precautions

It appears clearly that the waves' speed choice in the HLLC solver has dramatic consequences on method convergence in the low Mach number limit. It is also clear that the more M_{ref} tends to the local Mach number, in the low Mach limit, the better the accuracy is. Therefore, the best solution consists in setting the reference Mach number, M_{ref}, to the local one, M_i. But, as the artificial "sound speeds" (24) tend to wrong values when M tends to 0, the following function is used:

$$M^i_{ref} = \begin{cases} 1, & \text{if } M_i \geqslant 0.3, \\ M_i, & \text{if } 0.3 > M_i > M_{ref,min}, \\ M_{ref,min}, & \text{if } M_i \leqslant M_{ref,min}. \end{cases} \tag{42}$$

The upper limit, 0.3 has been chosen in reference to the "common" arbitrary barrier between a compressible and an incompressible flow. Nevertheless, depending on the applications, changing this limit might have some impacts on the solution. In the test cases considered in this paper, using 0.3 was appropriate.

The minimum Mach number, $M_{ref,min}$ is typically 10^{-2} or 10^{-3}. The preconditioned sound speeds must be computed with a unique M^*_{ref} at a given cell boundary for the Riemann problem resolution:

$$M^*_{ref} = Max\left(M^L_{ref}, M^R_{ref}\right) \tag{43}$$

where the superscripts "L" and "R" denote the left and right states of a cell boundary.

It is also important to report the computational cost to reach steady state on the previous computational example with this method. The stability restriction for such scheme is more restrictive than conventional CFL criterion for compressible flows. Indeed, the time step has to fulfil [48]:

$$\Delta t \leqslant CFLM_{ref,min} \frac{\Delta x}{Max(|u| + c)}. \tag{44}$$

This modified CFL restriction is due to the added dissipation by the modified wave speeds (29). It explains the computational costs reported in Tables 2 and 3.

The corresponding Godunov scheme with low Mach preconditioning is thus accurate but still expensive due to the time step restriction (44). It is thus mandatory to derive an implicit scheme.

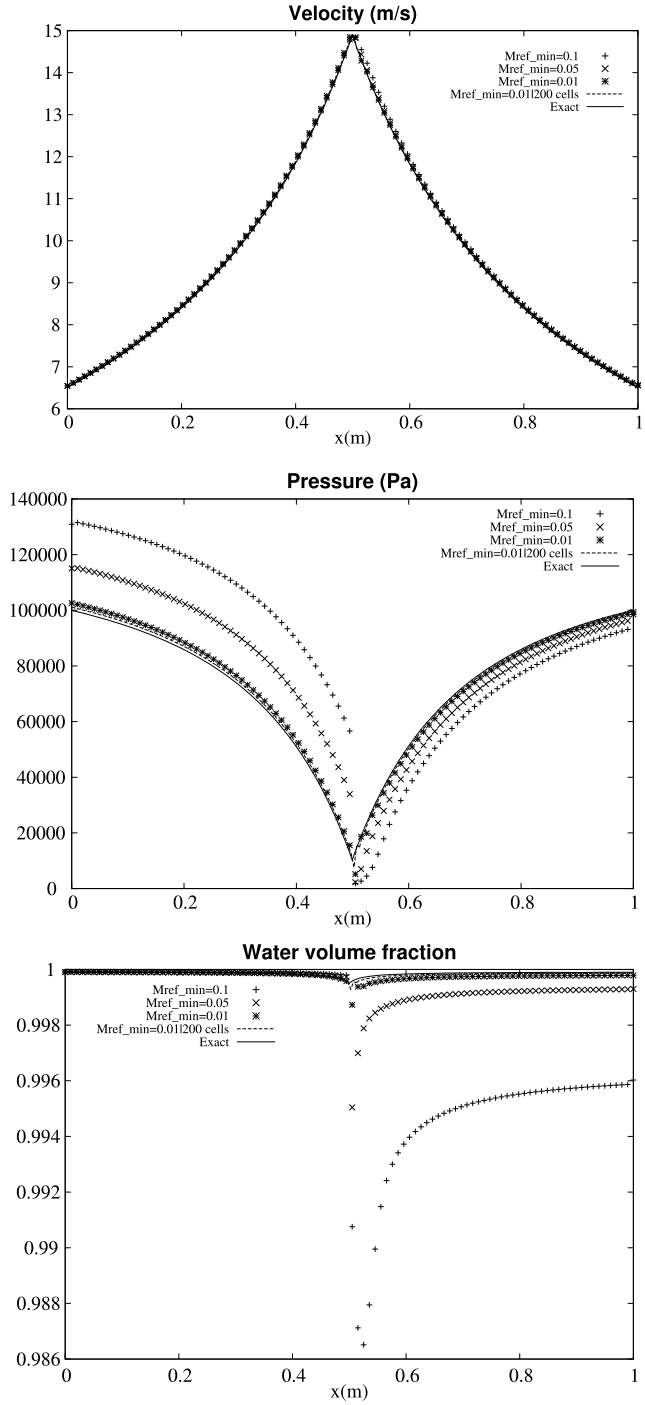

Fig. 5. Computed mixture velocity, mixture pressure, and water volume fraction profiles in the two-phase nozzle using different values of M_{ref} against the compressible exact solution. The error decreases dramatically as soon as M_{ref} is used and tends to the local Mach number.

5. Implicit scheme

5.1. Implicit scheme for the Euler equations

In order to overcome aforementioned stability restrictions, an implicit scheme has to be used. For the sake of simplicity, the implicit scheme is first presented for the Euler equations in 1D. Multi-D and multiphase extensions are addressed later.

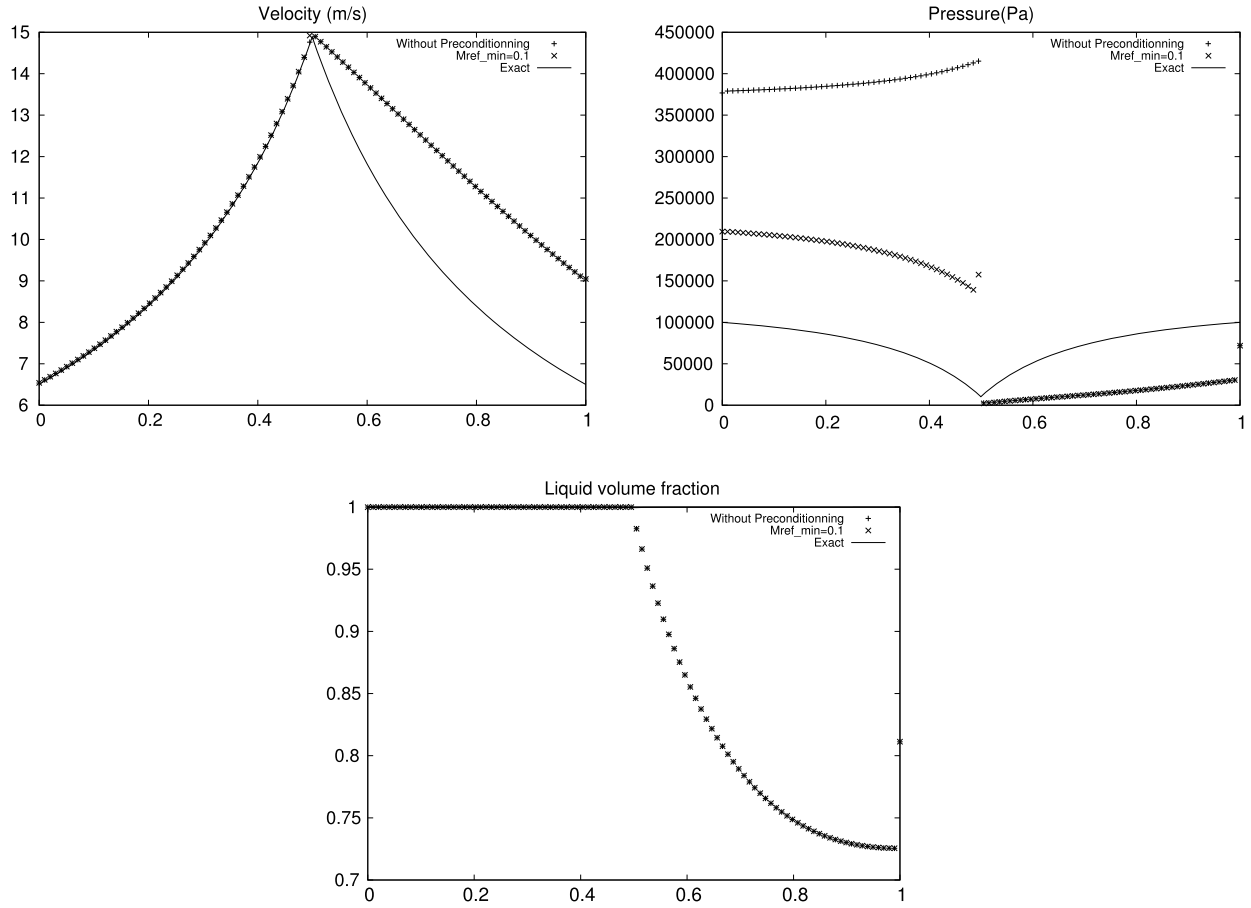

Fig. 6. Computed mixture pressure, velocity and water volume fraction profiles in the two-phase nozzle using Murrone and Guillard [45] low Mach preconditioning technique compared to the exact compressible solution. This technique clearly has convergence issues for two-phase solutions.

Table 2
Computational time versus $M_{ref,min}$ for the Laval *single phase* nozzle test problem with 100 cells.

$M_{ref,min}$	CPU
0.1	3 min 17 s
Minimum local Mach	1 h 23 min 12 s

Table 3
Computational time versus $M_{ref,min}$ for the Laval *two-phase* nozzle test problem with 100 and 200 cells.

$M_{ref,min}$	CPU
0.1	4 min 06 s
0.01	44 min
0.01	2 h 36 min (200 cells)

5.1.1. Implicit Godunov scheme

The implicit version of the Godunov scheme reads:

$$U_i^{n+1} - U_i^n = -\frac{\Delta t}{\Delta x}\left(F_{i+\frac{1}{2}}^{n+1} - F_{i-\frac{1}{2}}^{n+1}\right) \tag{45}$$

where the flux vectors $F_{i+\frac{1}{2}}^{n+1}$ and $F_{i-\frac{1}{2}}^{n+1}$ are computed according to variables at time t^{n+1}. Under the Taylor expansion, the flux vectors become:

$$F_{i+\frac{1}{2}}^{n+1} = F_{i+\frac{1}{2}}^{n} + \frac{\partial F_{i+\frac{1}{2}}}{\partial U_i}\Bigg)^n \left(U_i^{n+1} - U_i^n\right) + \frac{\partial F_{i+\frac{1}{2}}}{\partial U_{i+1}}\Bigg)^n \left(U_{i+1}^{n+1} - U_{i+1}^n\right), \tag{46}$$

$$F^{n+1}_{i-\frac{1}{2}} = F^{n}_{i-\frac{1}{2}} + \frac{\partial F_{i-\frac{1}{2}}}{\partial U_i}\Big)^n \left(U_i^{n+1} - U_i^n\right) + \frac{\partial F_{i-\frac{1}{2}}}{\partial U_{i-1}}\Big)^n \left(U_{i-1}^{n+1} - U_{i-1}^n\right). \tag{47}$$

Let's take the example of the right cell boundary. The corresponding flux, $F^n_{i+\frac{1}{2}}$, is solution of the Riemann problem and is consequently function of the left and right states: $F^n_{i+\frac{1}{2}} = F^*(U_i^n, U_{i+1}^n)$. The Riemann solver used here is the HLLC solver, already presented (64). Let's denote the variation:

$$\delta U_i = U_i^{n+1} - U_i^n. \tag{48}$$

Rewriting relations (45), (46) and (47) using (48), the following scheme is obtained:

$$\begin{aligned} &-\frac{\Delta t}{\Delta x}\frac{\partial F_{i-\frac{1}{2}}}{\partial U_{i-1}}\Big)^n \delta U_{i-1} + \delta U_i\left[I + \frac{\Delta t}{\Delta x}\frac{\partial F_{i+\frac{1}{2}}}{\partial U_i}\Big)^n - \frac{\Delta t}{\Delta x}\frac{\partial F_{i-\frac{1}{2}}}{\partial U_i}\Big)^n\right] + \frac{\Delta t}{\Delta x}\frac{\partial F_{i+\frac{1}{2}}}{\partial U_{i+1}}\Big)^n \delta U_{i+1} \\ &\quad = -\frac{\Delta t}{\Delta x}\left(F^n_{i+\frac{1}{2}} - F^n_{i-\frac{1}{2}}\right). \end{aligned} \tag{49}$$

It forms a block tridiagonal linear system composed of full matrices. This tridiagonal system can be solved either by direct or by iterative methods. We have implemented the Gauss–Siedel iterative method as well as a connexion with the PETSc libraries [49–51], which use the Krylov subspace method.

It is worth to mention that this Taylor expansion method is a particular case of the Newton–Raphson method which can be presented as follows. Let's consider the function $G(\delta U)$ whose components are $G_i(\delta U) = \delta U + \frac{\Delta t}{\Delta x}(F^{n+1}_{i+\frac{1}{2}} - F^{n+1}_{i-\frac{1}{2}})$. The goal is to solve,

$$G(\delta U) = 0. \tag{50}$$

As $F^{n+1}_{i+\frac{1}{2}}$ and $F^{n+1}_{i-\frac{1}{2}}$ are non-linear functions of δU_i, one way to solve this equation is to use the Newton–Raphson method, which, in this case, reads:

$$G\left(\delta U^{k+1}\right) = G\left(\delta U^k\right) + \left(\frac{\partial G(\delta U^k)}{\partial \delta U^k}\right)\left(\delta U^{k+1} - \delta U^k\right). \tag{51}$$

As the condition $G(\delta U^{k+1}) = 0$ has to be reached, the following formula is obtained:

$$\delta U^{k+1} = \delta U^k - \left[\left(\frac{\partial G(\delta U^k)}{\partial \delta U^k}\right)\right]^{-1} G\left(\delta U^k\right). \tag{52}$$

where δU^k represents δU at the k step of the iterative method. For practical applications, one or two iterations only are used.

The implicit Godunov type scheme needs an approximate Riemann solver to compute the numerical fluxes $F^n_{i\pm\frac{1}{2}}$ as well as the various flux derivatives. The HLLC flux (64) is used and the flux derivatives appearing in (49) are given by:

$$\frac{\partial F_{LR}}{\partial U_L} = \frac{1}{2}\frac{\partial F_L}{\partial U_L} - \frac{1}{2}\sum_j^{n_w} sign(\lambda_j)\frac{\partial \delta W_j}{\partial U_L}, \qquad \frac{\partial F_{LR}}{\partial U_R} = \frac{1}{2}\frac{\partial F_R}{\partial U_R} - \frac{1}{2}\sum_j^{n_w} sign(\lambda_j)\frac{\partial \delta W_j}{\partial U_R}. \tag{53}$$

The calculation details for the HLLC Riemann solver are given in Appendix C.

For the considered test cases shown in this paper, solving the linear system takes about 70% of the computation time.

5.1.2. Illustrations

To illustrate the implicit scheme efficiency, we consider the same test problem as before (Section 4.2.1). A coarse mesh with 100 grid points is considered. Corresponding results are shown in Fig. 7 at steady state.

As expected, the implicit scheme is numerically stable for larger time steps. It is worth to mention that the computational time is now 4 min, with a CFL coefficient equal to 15, to be compared to the computational time of 43 min needed by the explicit scheme, with stability condition (44).

5.1.3. Time accuracy

The previous sections have illustrated the implicit scheme ability to converge to exact steady solutions using low Mach number preconditioning. In order to check its time accuracy capabilities, a liquid–liquid shock tube test case is considered. The domain is a 1 m long shock tube containing two chambers separated by an interface at the location $x = 0.5$ m. In this tube, each chamber contains pure liquid water ($\gamma_{water} = 4.4$, $P_{\infty,water} = 600$ MPa) at an initial density of 1000 kg m^{-3}. The initial pressure in the left chamber is set equal to 1 MPa while the initial pressure in the right chamber is set equal to 0.1 MPa.

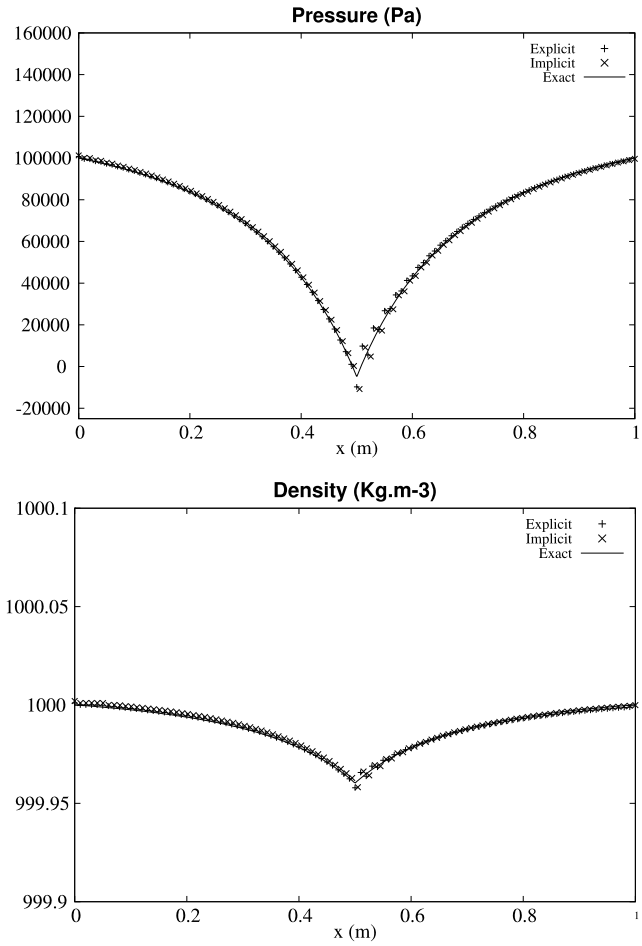

Fig. 7. Computed pressure and density profiles in the Laval liquid nozzle flow with $M_{ref} = M_i$ compared against the compressible exact solution. Implicit, explicit and exact solutions show excellent agreement.

The explicit and implicit with low Mach preconditioning numerical solutions are compared to the exact solution of the Euler equations at a physical time equals to $t = 0.15$ ms (Fig. 8). These computations are made on a mesh composed of 200 uniform cells with a CFL coefficient equal to 0.8 for the explicit low Mach computations and 8.0 for the implicit ones. These results show that the low Mach preconditioning preserves wave propagation. Indeed, although the results calculated with the implicit scheme and low Mach number preconditioning are clearly diffused, they predict the correct jumps through the shock and expansion wave as well as the correct mean wave positions. This time accuracy capability is of fundamental importance to predict cavitation instabilities in industrial systems as those illustrated in Figs. 12 and 15. These instabilities are closely linked to pressure wave propagation. The present method is clearly time accurate.

5.2. Multi-D extension

Multi-D extension of the method requires Riemann solver preconditioning as developed previously. Indeed, even if it has been argued that low Mach convergence difficulties were vanishing when using triangular cells [52,53] with conventional Godunov methods, this "miracle" strictly due to triangles was only possible for open domains, i.e in the absence of boundary conditions. This is not at all the case for practical applications. Therefore we address in the following a multi-D extension of the implicit method presented previously. Let's consider a cell, i, and denote by $V(i)$ its volume and by $Vo(i)$ the set of neighbouring and cells, as shown in Fig. 9.

Therefore, the implicit Godunov finite volumes scheme reads:

$$\left(U_i^{n+1} - U_i^n\right) = -\frac{\Delta t}{V(i)} \sum_{j \in Vo(i)} F_{i,j}^{n+1}. \tag{54}$$

Under similar notations as in 1D, the fluxes are expanded as follows:

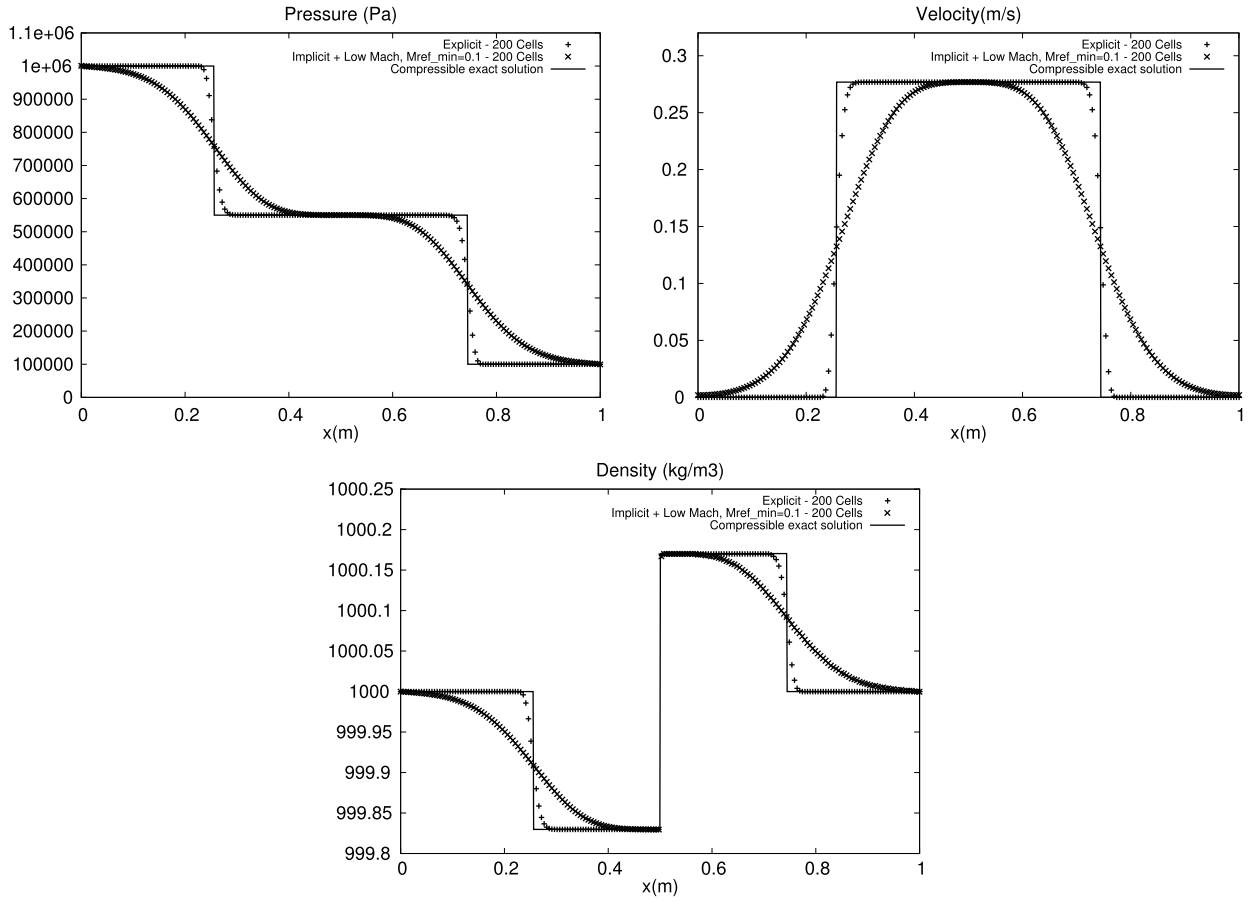

Fig. 8. Computed pressure, velocity and density profiles in the liquid–liquid shock tube with the conventional explicit Godunov scheme and the implicit scheme with low Mach preconditioning ($M_{ref,min} = 0.1$) compared against the compressible exact solution. The implicit scheme using low Mach preconditioning is clearly diffused but predicts the correct jumps through the shock and expansion wave.

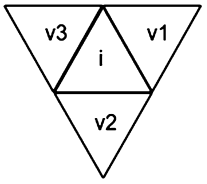

Fig. 9. Schematic representation of a triangular cell with its set of neighbours, $Vo(i) = \{V_1, V_2, V_3\}$.

$$F_{i,j}^{n+1} = F_{i,j}^{n} + \frac{\partial F_{i,j}}{\partial U_i}\Big)^n \left(U_i^{n+1} - U_i^n\right) + \frac{\partial F_{i,j}}{\partial U_j}\Big)^n \left(U_j^{n+1} - U_j^n\right). \tag{55}$$

Denoting the variation by $\delta U_i = U_i^{n+1} - U_i^n$ and using (55) in (54) the following scheme is obtained,

$$\left(I + \frac{\Delta t}{V(i)} \sum_{j \in Vo(i)} A_{ii}^j\right)\delta U_i + \frac{\Delta t}{V(i)} \sum_{j \in Vo(i)} \left(A_{ij}^j \delta U_j\right) = -\frac{\Delta t}{V(i)} \sum_{j \in Vo(i)} F_{i,j}^{n+1} \tag{56}$$

with,

$$A_{ii}^j = \frac{\partial F_{i,j}}{\partial U_i}\Big)^n, \qquad A_{ij}^j = \frac{\partial F_{i,j}}{\partial U_j}\Big)^n.$$

In compact form it reads,

$$M\delta U = D,$$

where,

$$\delta U = \begin{bmatrix} \delta U_1 \\ . \\ . \\ . \\ \delta U_N \end{bmatrix}, \qquad D = \begin{bmatrix} . \\ . \\ -\frac{\Delta t}{V(i)} \sum_{j \in Vo(i)} F_{i,j}^{n+1} S(ij) \\ . \\ . \end{bmatrix}.$$

The M matrix shape depends on the number of faces per cell. In order save computational time, the sparse character of the M matrix has to be exploited. In this work, the CSC (Compressed Sparse Column) method is used, which is detailed in [54].

Higher order extension of the method is detailed in Appendix D.

5.3. Implicit scheme for the two-phase flow model

In this section, the implicit scheme for the hyperbolic two-phase flow model is addressed. The model under consideration corresponds to system (6) without relaxation terms. It is considered hereafter in 1D for the sake of simplicity. These equations can be arranged in two sets: Conservative equations on one hand and non-conservatives equations on the other hand. The conservative set of equations reads:

$$\frac{\partial \Omega}{\partial t} + \frac{\partial F(U)}{\partial x} = 0. \tag{57}$$

The non-conservative set of equations reads:

$$\frac{\partial V}{\partial t} + \frac{\partial G(U)}{\partial x} + H(U)\frac{\partial u}{\partial x} = 0 \tag{58}$$

where,

$$U = \begin{pmatrix} \Omega \\ V \end{pmatrix}, \qquad \Omega = \begin{pmatrix} \alpha_1\rho_1 \\ \alpha_1\rho_2 \\ \rho \mathbf{u} \\ \rho E \end{pmatrix}, \qquad V = \begin{pmatrix} \alpha_1 \\ \alpha_1\rho_1 e_1 \\ \alpha_2\rho_2 e_2 \end{pmatrix} \tag{59}$$

and,

$$F(U) = \begin{pmatrix} \alpha_1\rho_1\mathbf{u} \\ \alpha_1\rho_2\mathbf{u} \\ \rho\mathbf{u}^2 + P \\ (\rho E + P)\mathbf{u} \end{pmatrix}, \qquad G(U) = \begin{pmatrix} \alpha_1\mathbf{u} \\ \alpha_1\rho_1 e_1\mathbf{u} \\ \alpha_2\rho_2 e_2\mathbf{u} \end{pmatrix}, \qquad H(U) = \begin{pmatrix} -\alpha_1 \\ \alpha_1 p_1 \\ \alpha_2 p_2 \end{pmatrix}. \tag{60}$$

The implicit scheme derived previously for the Euler equations is used for the conservative system with some modifications. Indeed, the pressure, P, and the mixture total energy, E, are now functions of ρ, e, α_1, α_2 (7). Therefore, the derivatives involved in the implicit flux computation are more complex. Their expressions are given in Appendix E. Most of the efforts are focused on the implicit scheme for the non-conservative system. Approximating (8) implicitly reads:

$$V_i^{n+1} = V_i^n - \frac{\Delta t}{\Delta x}\left(G_{i+\frac{1}{2}}^{*,n+1} - G_{i-\frac{1}{2}}^{*,n+1} + H(U)_i^{n+1}\left(u_{i+\frac{1}{2}}^{*,n+1} - u_{i-\frac{1}{2}}^{*,n+1}\right)\right). \tag{61}$$

Using the same development as previously (46)–(47), the following scheme is obtained:

$$\begin{aligned} &-\frac{\Delta t}{\Delta x}\left[\frac{\partial G_{i-\frac{1}{2}}}{\partial U_{i-1}} + H_i^n \frac{\partial u_{i-\frac{1}{2}}^*}{\partial U_{i-1}}\right]\delta V_{i-1} \\ &\quad + \left[I + \frac{\Delta t}{\Delta x}\left(\frac{\partial G_{i+\frac{1}{2}}^n}{\partial U_i} - \frac{\partial G_{i-\frac{1}{2}}^n}{\partial U_i} + H_i^n\left[\frac{\partial u_{i+\frac{1}{2}}^*}{\partial U_i} - \frac{\partial u_{i-\frac{1}{2}}^*}{\partial U_i}\right] + \left(u_{i+\frac{1}{2}}^* - u_{i-\frac{1}{2}}^*\right)\frac{\partial H_i^n}{\partial U_i}\right)\right]\delta V_i \\ &\quad + \frac{\Delta t}{\Delta x}\left[\frac{\partial G_{i+\frac{1}{2}}}{\partial U_{i+1}} + H_i^n \frac{\partial u_{i+\frac{1}{2}}^*}{\partial U_{i+1}}\right]\delta V_{i+1} \\ &= -\frac{\Delta t}{\Delta x}\left(G_{i+\frac{1}{2}}^{*,n} - G_{i-\frac{1}{2}}^{*,n} + H_i^n\left(u_{i+\frac{1}{2}}^{*,n} - u_{i-\frac{1}{2}}^{*,n}\right)\right). \end{aligned} \tag{62}$$

The various expressions for the derivatives are detailed in Appendix F.

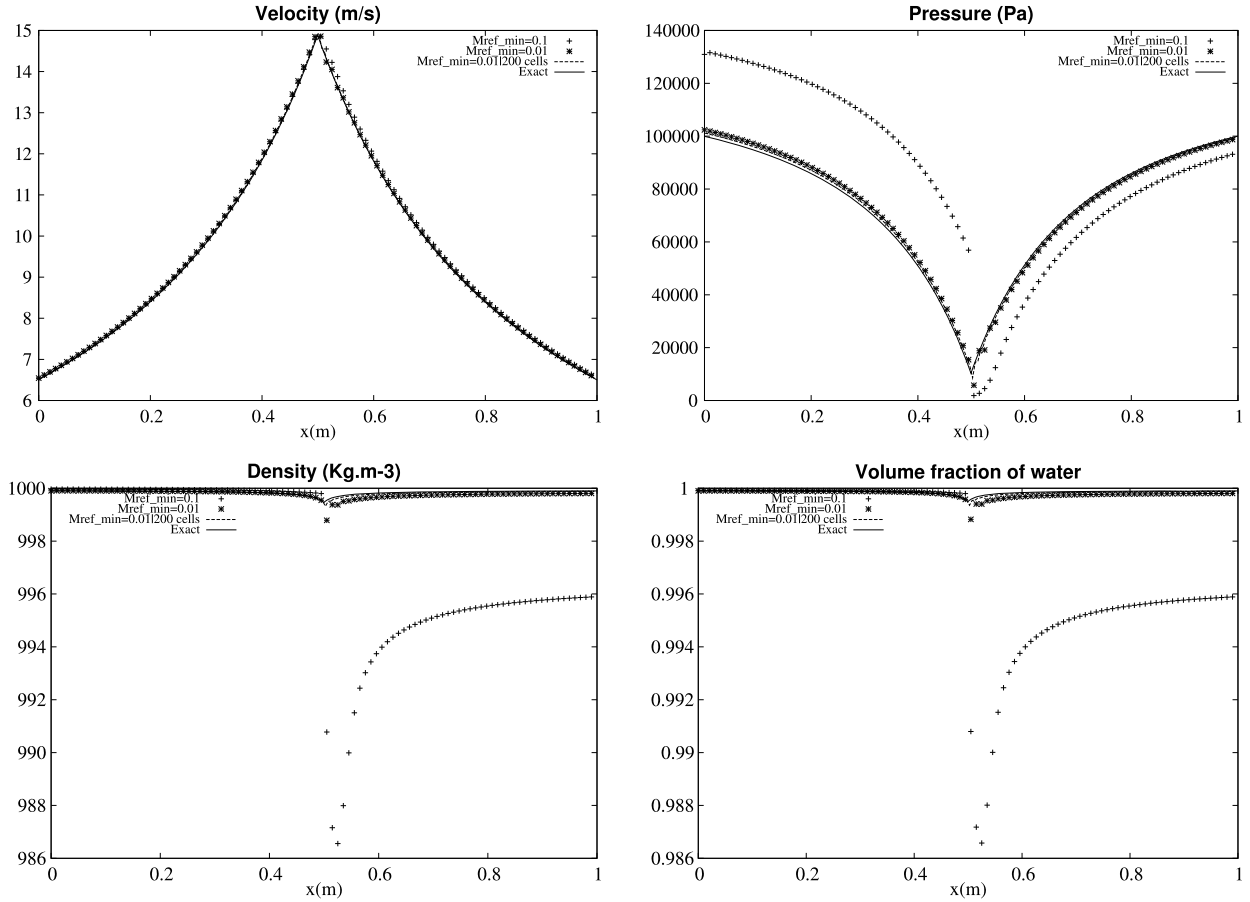

Fig. 10. Computed mixture pressure, velocity, density and water volume fraction profiles in the two-phase nozzle using different values of $M_{ref,min}$ against the compressible exact solution. The exact solution is reached when $M_{ref,min}$ is equal to 0.01.

Table 4
Computational time versus $M_{ref,min}$ for the Laval *two-phase* nozzle test problem with the implicit scheme.

$M_{ref,min}$	CPU (Implicit scheme)	Implicit CFL	Explicit CFL
0.1	46 s	30.0	0.9
0.01	8 min 45 s (200 cells)	150.0	0.9

6. Illustrations and validations

6.1. One-dimensional two-phase nozzle flow

To illustrate the behaviour of the two-phase implicit scheme, we consider the same two-phase nozzle flow test as before (Section 4.2.2). The numerical solution has been computed using different values of $M_{ref,min}$ (0.1 and 0.01) as well as two different meshes (100 and 200 cells). Corresponding results are shown in Fig. 10 at steady state.

The implicit scheme has the same behaviour and accuracy as the explicit version. The corresponding computational cost is reported in Table 4, with stability condition (44).

Compared to explicit calculation times (Table 3), considerable saving appear as the implicit scheme reduces the computation times cost by a factor of 18. To conclude, the implicit scheme presented in the previous section is efficient and accurate for two-phase flow calculations. Multi-D two-phase examples are addressed in the next subsection.

6.2. 2D computations of cavitating flows in Venturi channels

In this subsection, 2D two-phase nozzle flow computation is addressed. We first present the geometry and the various flow parameters. Then, numerical results are compared against experimental records.

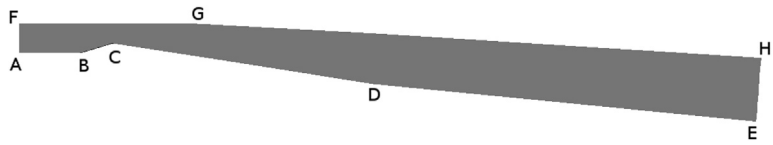

Fig. 11. LEGI 8° Venturi geometry.

Table 5
Venturi 8° points coordinates.

	X (abscissa) (m)	Y (m)		X (abscissa) (m)	Y (m)
A	0	0	E	1.225	−0.114
B	0.1	0	F	0	0.0488
C	0.153	0.0157	G	0.271	0.0488
D	0.588	−0.0517	H	1.233	−0.00845

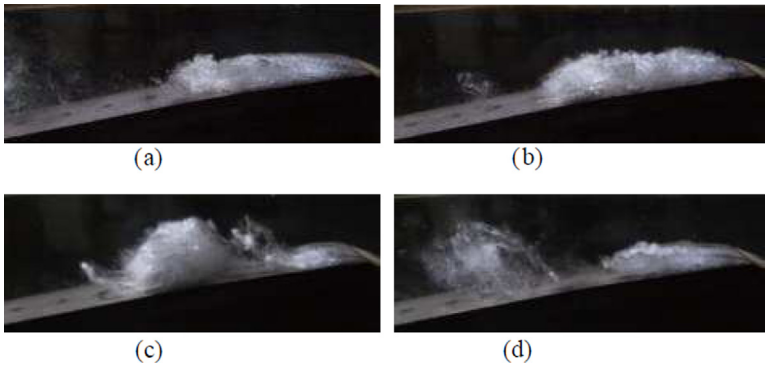

Fig. 12. Instantaneous pictures of a break off cycle in the 8° Venturi channel of LEGI. Courtesy of S. Barre, LEGI, Grenoble, France.

6.2.1. Test problem

The experimental facility has been built at LEGI Laboratory, Grenoble, France by the group led by S. Barre. The test section corresponds to a Venturi channel with a nozzle divergent inclined at an angle of 8°. The geometry is shown in Fig. 11.

The corresponding point coordinates are given in Table 5.

As phase transition occurs at the throat, heat and mass transfer have to be considered. These effects are accounted for by considering extra relaxation effects in addition to pressure relaxation. Indeed, as detailed in Saurel et al. [2], temperature and Gibbs free energy relaxation have to be considered. Appropriate relaxation solver is summarized in Appendix G. Simulating phase transition requires appropriate EOS parameters. The fluids considered correspond to liquid water and water vapour, with the following SG EOS (4) parameters: $\gamma_{liq} = 1.234$, $P_{\infty,liq} = 2532.302$ atm, $\gamma_{vap} = 1.316$ and $P_{\infty,vap} = 0$ Pa. These parameters have been computed following the method detailed in [35].

Mass inflow rate and stagnation enthalpy are imposed and a prescribed pressure is imposed at the outlet. The imposed conditions at the left inlet are the following,

$$m = 7514.917\ \mathrm{kg\,m^{-2}\,s^{-1}}, \qquad \rho_{liq} = 1067.566\ \mathrm{kg\,m^{-3}}, \qquad \rho_{vap} = 0.387\ \mathrm{kg\,m^{-3}},$$
$$\alpha_{liq} = 0.999, \qquad P = 51\,825\ \mathrm{Pa}$$

while, at the right outlet, the prescribed pressure is $P = 72\,025$ Pa.

6.2.2. Experimental results

The 8° Venturi channel of Fig. 11 has been used at LEGI (Grenoble, France) to study cavitating flows. With the boundary conditions reported in the previous subsection, a periodic flow is observed, as shown in Fig. 12. In the first stage of the cycle (a), a cavitation sheet is attached to the throat and grows. In a second stage, the sheet reaches its maximum length (b) and breaks in two parts (c). At the end, the downstream part is swept along within the stream and starts to collapse while the attached part starts another cycle (d). The mean attached cavity length value is 45 ± 5 mm while the quasi-periodic vapour clouds shedding frequency is about 45 Hz. The cloud shedding frequency is calculated using spectral analysis of pressure measurement in the Venturi divergent.

6.2.3. Numerical results

A 2D unstructured mesh containing 52 450 cells is used, as shown in Fig. 13. The grid is refined at the throat in order to capture the cavitation pocket. The average cell size is 0.013 mm at the throat and 0.08 mm elsewhere.

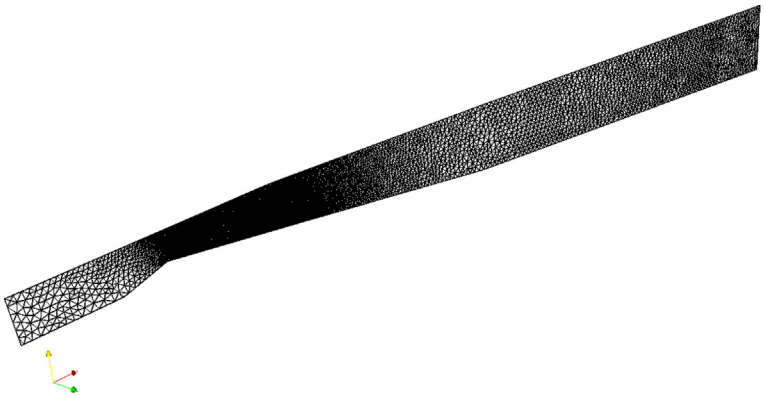

Fig. 13. Venturi 8° 2D unstructured mesh.

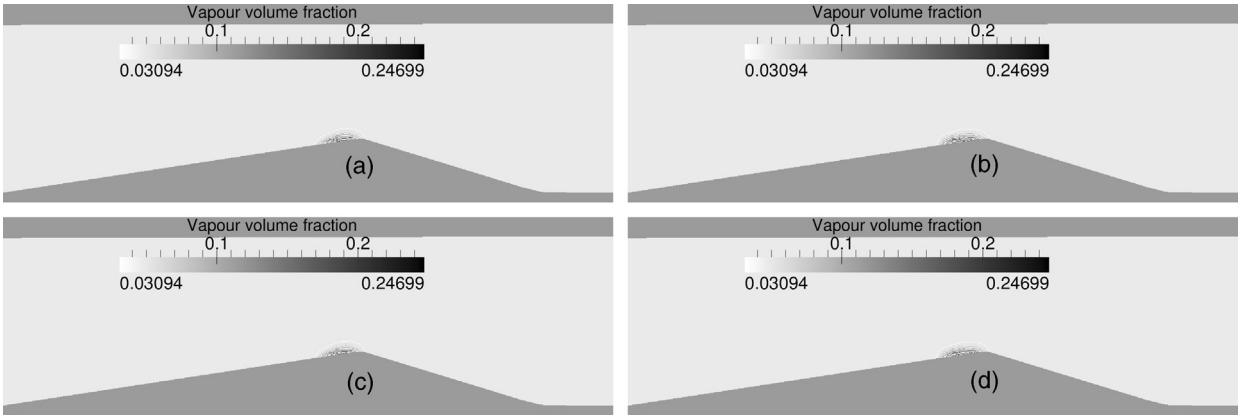

Fig. 14. Computed contours of volume fraction of water vapour without low Mach preconditioning. The computed results do not present any shedding and the vapour pocket size as well as the computed flow are in complete disagreement with the experiments. The flow is coming from right to left.

We first address again the remark mentioned at the beginning of Section 5.2, related to the "triangle miracle" [52, 53]. With the mesh shown in Fig. 13, made of triangles, the two-phase 2D explicit scheme is used without low Mach preconditioning to reach 1.8 s of physical time. As shown in the volume fraction contours of Fig. 14, the obtained pockets does not present any cloud shedding and they only contain around 27% of vapour. The vapour pocket size as well as the observed behaviour are in total disagreement with the experimental results. Indeed, the mean vapour pocket length is about 18 mm and no oscillatory behaviour is observed.

We now consider the same mesh with the two-phase 2D implicit scheme along with the two-phase low Mach preconditioning ($M_{ref,min}$ is set to 0.04). Using a cluster with 24 CPU 1.8 s of physical time is reached in about 97 h with an average CFL coefficient equal to 28. It's worth to mention that the projected calculation time (obtained after running the simulation for two days) using an explicit scheme with the same low Mach preconditioning is about 5107 h ($\simeq$ 7 months). Therefore, using the implicit scheme allows for a projected acceleration factor of about 53.

This physical time was long enough to obtain a quasi-stationary flow with quasi-periodic vapour cloud shedding. An example of the obtained cloud shedding is shown in the volume fraction contours of Fig. 15. Moreover, the velocity magnitude and Mach number contours at the end of the cycle are shown in Fig. 16. The Mach number is built using the equilibrium sound speed. From Figs. 14 and 15, it appears that the quasi-incompressible behaviour of the liquid must be considered, otherwise cavitation pockets present huge discrepancies. But, its is also clear that compressible effects are also important, as shown in Fig. 16. This illustrates the difficulty of cavitating flows computations. A pressure signal is also recorded using a numerical gauge located in the middle of the $\overline{EH}$ segment, at the end of the Venturi divergent (Fig. 11). Examining the water vapour volume fraction contours oscillations, a vapour pocket shedding frequency of about 43 Hz is determined. In order to check this observed frequency, a spectral analysis of the recorded pressure signal was performed. The obtained spectrum is shown in Fig. 17. The maximum intensity is reached for frequencies between 40 and 50 Hz, which is in very good agreement with the observed clouds shedding frequency based on the vapour pocket oscillations. By performing measurements during every cycle, an average attached cavity length of about 45 mm has been measured from the computations. These results show again very good agreement with the experiments. Indeed, experimental measurements gave a mean attached cavity length equals to 45 ± 5 mm.

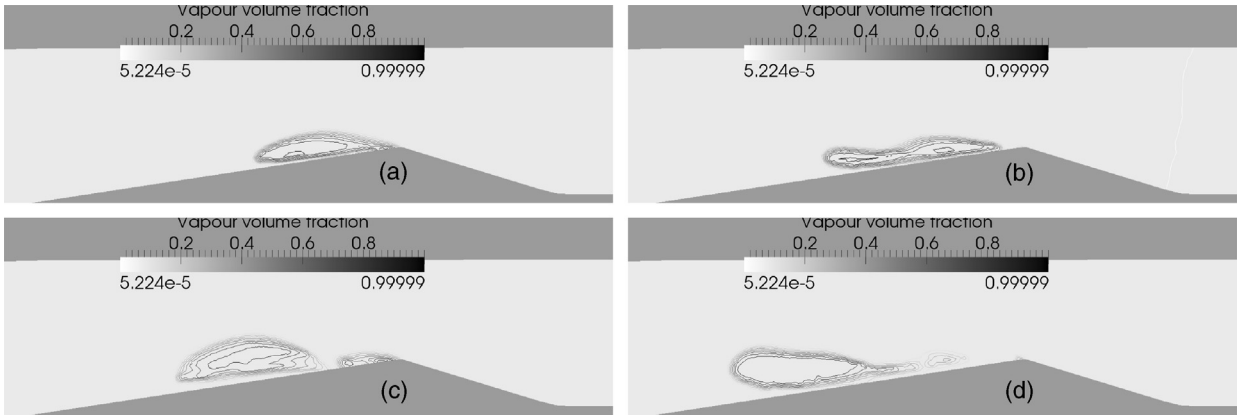

Fig. 15. Computed contours of volume fraction of water vapour. This example of the computed break off cycles shows the same four different parts as those observed during the experimental studies and shown in Fig. 12. The mean attached cavity length is about 45 mm, in perfect agreement with the experiments.

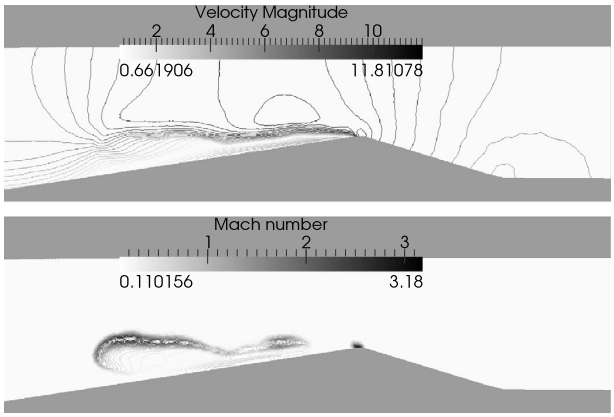

Fig. 16. Velocity magnitude and Mach number contours at the end of the cycle (d). Throat close-up. The Mach number is built with the equilibrium sound speed.

An important remark regarding the modelling of such flows appears. It is possible to reproduce the large structures of such cavitating flows without having recourse to adjustable parameter nor turbulence modelling. The present results show that,

- a model in agreement with the fundamental principles of total energy conservation and entropy inequality, and,
- an algorithm suited for two-phase all Mach number conditions,

reproduce with high fidelity the experiments, at least in the present conditions.

7. Conclusion

The Turkel preconditioned formulation has been used in the Riemann problem solution determination and embedded in the Godunov method with HLLC scheme, in both explicit and implicit versions. This variant of the Turkel method, due to Guillard and Viozat [19], has shown particular efficiency for all Mach number single phase flow conditions. It has been extended to the two-phase flow model of Kapila et al. [1], particularly suited for interfacial flows [3] as well as cavitating flows [2]. Compared to conventional cavitating flow models widely used in industry, this model conserves energy. Also, phase transition is modelled in a thermodynamically consistent way. The preconditioning method requires mild modifications on the internal energy jumps conditions in the Riemann solver that have important consequences on method convergence. The method has been validated against exact 1D solutions and experimental 2D cavitating Venturi flows. Without using any adjustable parameter, the method has shown its ability to reproduce many challenging features of cavitating flows.

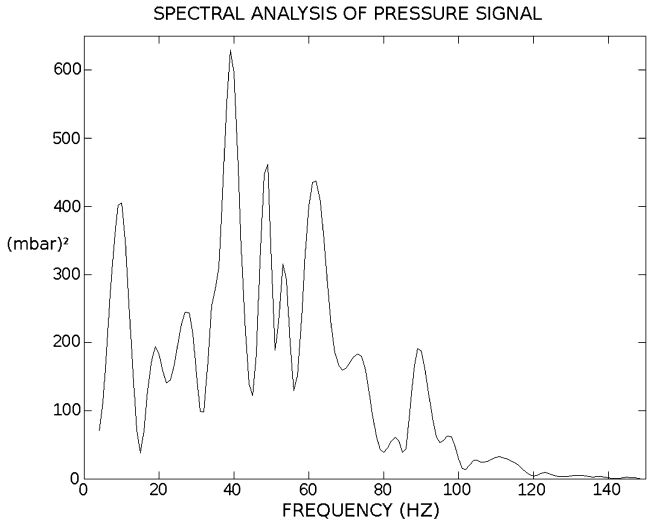

Fig. 17. Spectral analysis of the recorded pressure signal using a pressure gauge located at the end of the Venturi divergent. The obtained spectrum shows maximum intensity for frequencies between 40 and 50 Hz. This is in excellent agreement with the computed cloud shedding frequency of 43 Hz and in excellent agreement with the experimental frequency of 45 ± 5 Hz.

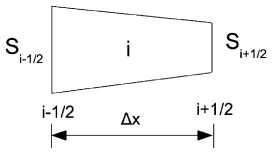

Fig. 18. Nozzle computational cell i with its two cell boundaries, $i+1/2$ and $i-1/2$.

Acknowledgements

The first author has been partly supported by CNES and SNECMA. Drs. B. Vieille, S. Petitot and P. Boivin are gratefully acknowledged. The authors would like to acknowledge fruitful discussions and work with Dr. F. Petitpas.

Appendix A. Godunov–HLLC scheme for the Euler equations in ducts of smooth varying cross sections

Let's consider a computational cell corresponding to an arbitrary control volume inside a nozzle, as shown in Fig. 18. The conventional 1D Godunov scheme for ducts of smooth varying cross sections reads:

$$U_i^{n+1} = U_i^n - \frac{\Delta t}{V_i}\left(F^*_{i+\frac{1}{2}} S_{i+\frac{1}{2}} - F^*_{i-\frac{1}{2}} S_{i-\frac{1}{2}}\right) + \frac{\Delta t}{V_i} G_i (S_{i+\frac{1}{2}} - S_{i-\frac{1}{2}}) \tag{63}$$

with

$$U = \begin{pmatrix} \rho \\ \rho u \\ \rho E \end{pmatrix}, \qquad F = \begin{pmatrix} \rho u \\ \rho u^2 + p \\ (\rho E + p)u \end{pmatrix}, \qquad G_i = \begin{pmatrix} 0 \\ p_i^n \\ 0 \end{pmatrix}$$

where:

- U represents the conservative variables vector,
- F represents the flux vector,
- S represents the cell boundary surface,
- V_i represents the cell volume.

This basic first-order version is used to avoid artefacts in the various computational test.

The HLLC Riemann solver (Toro et al. [34]) is used to compute the inter-cell flux F^* (see Fig. 19). At cell boundary $i+\frac{1}{2}$, it reads:

$$F_{L,R} = \frac{1}{2}(F_L + F_R) - sign(S_L)\frac{S_L}{2}\left(U_L^* - U_L\right) - sign(S_M)\frac{S_M}{2}\left(U_R^* - U_L^*\right) - sign(S_R)\frac{S_R}{2}\left(U_R - U_R^*\right). \tag{64}$$

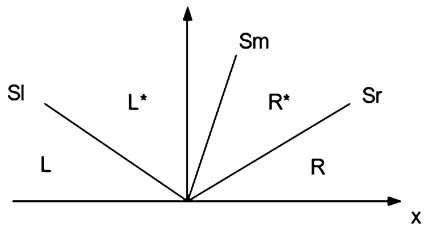

Fig. 19. Schematization of the Riemann problem for the Euler equations under HLLC approximation and associated wave speeds.

The subscripts L and R denote the left and right state of the Riemann problem, respectively. The wave speeds S_R and S_L are estimated with Davis approximation [55],

$$S_R = Max(u_R + c_R, u_L + c_L), \qquad S_L = Max(u_R - c_R, u_L - c_L), \tag{65}$$

while S_M is estimated under HLL [56] approximation,

$$S_M = \frac{S_R U_R(2) - S_L U_L(2) - (F_R(2) - F_L(2))}{S_R U_R(1) - S_L U_L(1) - (F_R(1) - F_L(1))}. \tag{66}$$

The states U_L^* and U_R^* are determined with the help of Rankine–Hugoniot jump relations across the S_R and S_L waves,

$$F_L^* - S_L U_L^* = F_L - S_L U_L, \qquad F_R^* - S_R U_R^* = F_R - S_R U_R, \tag{67}$$

and interface relations, $u_L^* = u_R^* = S_M$ and $p_L^* = p_R^* = p^*$, across the contact wave. It results in:

$$U_L^* = \frac{1}{S_M - S_L}\left[F_L - S_L U_L - \left(0, p^*, S_M.p^*\right)^T\right], \qquad U_R^* = \frac{1}{S_M - S_R}\left[F_R - S_R U_R - \left(0, p^*, S_M.p^*\right)^T\right]. \tag{68}$$

Appendix B. Exact steady two-phase nozzle solution with imposed mass flow rate and stagnation enthalpy

In many practical situations, the mass flux m_0 is imposed as well as the stagnation enthalpy H_0. For two-phase flows, the mixture enthalpy reads:

$$H_0 = Y_{0,1} h_{0,1} + Y_{0,2} h_{0,2} + \frac{1}{2} u_0^2. \tag{69}$$

It means that the mass fractions have to be imposed, as well as the volume fraction of one of the phases, $\alpha_{0,1}$, for example. It is thus necessary to impose m_0, $h_{k,0}$, $Y_{k,0}$ and $\alpha_{1,0}$. Another option being to impose m_0, P_0, $\rho_{k,0}$ and $\alpha_{1,0}$. The exact solution determination with such boundary conditions follows the same methodology as the one detailed previously in [40] for single phase flows.

Outlet state determination for subsonic isentropic flows. The outlet pressure is prescribed and denoted by P_{out}. Using the SG EOS (4) the phase total enthalpy is expressed at the outlet as:

$$h_{k,0} = \frac{\gamma_k (P_{out} + P_{\infty,k}) v_{k,out}}{(\gamma_k - 1)} + \frac{1}{2} u_{out}^2. \tag{70}$$

With the help of the mass flow rate conservation ($m_0 = \rho_{out} A_{out} u_{out}$) and the mixture density definition ($\frac{1}{\rho_{out}} = Y_{1,0} v_{1,out} + Y_{2,0} v_{2,out}$), the two following equations are obtained:

$$h_{1,0} = \frac{\gamma_1 (P_{out} + P_{\infty,1}) v_{1,out}}{(\gamma_1 - 1)} + \frac{1}{2}\left(\frac{m_0}{A_{out}}\right)^2 (Y_{1,0} v_{1,out} + Y_{2,0} v_{2,out})^2, \tag{71}$$

$$h_{2,0} = \frac{\gamma_2 (P_{out} + P_{\infty,2}) v_{2,out}}{(\gamma_2 - 1)} + \frac{1}{2}\left(\frac{m_0}{A_{out}}\right)^2 (Y_{1,0} v_{1,out} + Y_{2,0} v_{2,out})^2. \tag{72}$$

Combining these two relations, an expression linking $v_{1,out}$ and $v_{2,out}$ is obtained:

$$v_{1,out} = \frac{(\gamma_1 - 1)}{\gamma_1 (P_{out} + P_{\infty,1})}\left[h_{1,0} - h_{2,0} + \frac{\gamma_2 (P_{out} + P_{\infty,2}) v_{2,out}}{(\gamma_2 - 1)}\right]. \tag{73}$$

Using this expression in relation (72), a second order polynomial in $v_{2,out}$ is obtained. The positive solution, $v_{1,out}$ is retained. Once $v_{1,out}$ and $v_{2,out}$ are known, the mixture density at the outlet section is obtained by,

$$\frac{1}{\rho_{out}} = Y_{1,0} v_{1,out} + Y_{2,0} v_{2,out} \tag{74}$$

and the outlet velocity is deduced by,

$$u_{out} = \frac{m_0}{\rho_{out} A_o}. \tag{75}$$

Last, the volume fractions are determined with the help of mass fractions conservation,

$$\alpha_{k,0} = Y_{k,0} \rho_{out} v_{k,out}. \tag{76}$$

Variables state determination in an arbitrary cross section. The flow is isentropic between a section of arbitrary area (A) and the outlet section. Thus, writing the phase total enthalpy conservation between a section of arbitrary area and the outlet gives the following relation:

$$h_{k,out} = \frac{\gamma_k (P + P_{\infty,k}) v_k(P)}{(\gamma_k - 1)} + \frac{1}{2}\left(\frac{m_0}{A}\right)^2 \left(Y_{1,0} v_{1,out}(P) + Y_{2,0} v_{2,out}(P)\right)^2. \tag{77}$$

The mixture pressure, P, is therefore determined by solving one of these relations using the Newton–Raphson method. Once P is known, the phase densities are determined using phases isentropes while the other variables are computed as previously.

Appendix C. HLLC Riemann solver derivatives

The HLLC approximate Riemann solver is recalled hereafter in the context of the Euler equations, where U_L^* and U_R^* are defined by relation (68):

$$F_{L,R} = \frac{1}{2}(F_L + F_R) - sign(S_L)\frac{S_L}{2}\left(U_L^* - U_L\right) - sign(S_M)\frac{S_M}{2}\left(U_R^* - U_L^*\right) - sign(S_R)\frac{S_R}{2}\left(U_R - U_R^*\right).$$

The flux vector derivatives are given by:

$$\frac{\partial F_{LR}}{\partial U_L} = \frac{1}{2}\frac{\partial F_L}{\partial U_L} - sign(S_L)\frac{S_L}{2}\left(\frac{\partial U_L^*}{\partial U_L} - 1\right) - sign(S_M)\frac{S_M}{2}\left(\frac{\partial (U_R^* - U_L^*)}{\partial U_L}\right) + sign(S_R)\frac{S_R}{2}\left(\frac{\partial U_R^*}{\partial U_L}\right), \tag{78}$$

$$\frac{\partial F_{LR}}{\partial U_R} = \frac{1}{2}\frac{\partial F_R}{\partial U_R} - sign(S_L)\frac{S_L}{2}\frac{\partial U_L^*}{\partial U_R} - sign(S_M)\frac{S_M}{2}\left(\frac{\partial (U_R^* - U_L^*)}{\partial U_R}\right) - sign(S_R)\frac{S_R}{2}\left(1 - \frac{\partial U_R^*}{\partial U_R}\right) \tag{79}$$

where:

$$\frac{\partial U_L^*}{\partial U_L} = \frac{(\frac{\partial F_L}{\partial U_L} - S_L - \frac{\partial}{\partial U_L}(0, P^*, S_M.P^*)^T)(S_M - S_L) - (F_L - S_L U_L - (0, P^*, S_M.P^*)^T)\frac{\partial S_M}{\partial U_L}}{(S_M - S_L)^2}, \tag{80}$$

$$\frac{\partial U_L^*}{\partial U_R} = \frac{-\frac{\partial}{\partial U_L}((0, P^*, S_M.P^*)^T)(S_M - S_L) - (F_L - S_R U_L - (0, P^*, S_M.P^*)^T)\frac{\partial S_M}{\partial U_R}}{(S_M - S_L)^2}, \tag{81}$$

$$\frac{\partial U_R^*}{\partial U_L} = \frac{-\frac{\partial}{\partial U_L}((0, P^*, S_M.P^*)^T)(S_M - S_R) - (F_R - S_R U_R - (0, P^*, S_M.P^*)^T)\frac{\partial S_M}{\partial U_L}}{(S_M - S_R)^2}, \tag{82}$$

$$\frac{\partial U_R^*}{\partial U_R} = \frac{(\frac{\partial F_R}{\partial U_R} - S_R - \frac{\partial}{\partial U_R}(0, P^*, S_M.P^*)^T)(S_M - S_R) - (F_R - S_R U_R - (0, P^*, S_M.P^*)^T)\frac{\partial S_M}{\partial U_R}}{(S_M - S_R)^2}. \tag{83}$$

Using relations (67), and $P_L^* = P_R^* = P^*$, two expressions for P^* are obtained:

$$P^* = F_L(2) - S_L U_L(2) - S_M\left(F_L(1) - S_L U_L(1)\right), \qquad P^* = F_R(2) - S_R U_R(2) - S_M\left(F_R(1) - S_R U_R(1)\right). \tag{84}$$

Nevertheless, in order to compute a more precise pressure derivative, the following average expression is used for P^*:

$$P^* = \frac{F_R(2) - S_R U_R(2) - S_M(F_R(1) - S_R U_R(1)) + F_L(2) - S_L U_L(2) - S_M(F_L(1) - S_L U_L(1))}{2}. \tag{85}$$

It results in the following pressure derivatives:

$$\frac{\partial P^*}{\partial U_L} = \frac{1}{2}\left[\frac{\partial F_L(2)}{\partial U_L} - S_L(0,1,0)^T - S_M\left(\frac{\partial F_L(1)}{\partial U_L} - S_L(1,0,0)^T\right) - \left(F_L(1) - S_L U_L(1)\right)\frac{\partial S_M}{\partial U_L}\right], \tag{86}$$

$$\frac{\partial P^*}{\partial U_R} = \frac{1}{2}\left[\frac{\partial F_R(2)}{\partial U_R} - S_R(0,1,0)^T - S_M\left(\frac{\partial F_R(1)}{\partial U_R} - S_R(1,0,0)^T\right) - (F_R - S_R U_R)\frac{\partial S_M}{\partial U_R}\right], \tag{87}$$

$$S_M = \frac{S_R U_R(2) - S_L U_L(2) - (F_R(2) - F_L(2))}{S_R U_R(1) - S_L U_L(1) - (F_R(1) - F_L(1))}, \tag{88}$$

$$\begin{aligned}\frac{\partial S_M}{\partial U_L} = {} & \frac{(\frac{\partial F_L(2)}{\partial U_L} - S_L\frac{\partial U_L(2)}{\partial U_L})(S_R U_R(1) - S_L U_L(1) - (F_R(1) - F_L(1)))}{(S_R U_R(1) - S_L U_L(1) - (F_R(1) - F_L(1)))^2} \\ & - \frac{(S_R U_R(2) - S_L U_L(2) - (F_R(2) - F_L(2)))(\frac{\partial F_L(1)}{\partial U_L} - S_L\frac{\partial U_L(1)}{\partial U_L})}{(S_R U_R(1) - S_L U_L(1) - (F_R(1) - F_L(1)))^2},\end{aligned} \tag{89}$$

$$\begin{aligned}\frac{\partial S_M}{\partial U_R} = {} & \frac{(S_R\frac{\partial U_R(2)}{\partial U_R} - \frac{\partial F_R(2)}{\partial U_R})(S_R U_R(1) - S_L U_L(1) - (F_R(1) - F_L(1)))}{(S_R U_R(1) - S_L U_L(1) - (F_R(1) - F_L(1)))^2} \\ & - \frac{(S_R U_R(2) - S_L U_L(2) - (F_R(2) - F_L(2)))(S_R\frac{\partial U_R(1)}{\partial U_R} - \frac{\partial F_R(1)}{\partial U_R})}{(S_R U_R(1) - S_L U_L(1) - (F_R(1) - F_L(1)))^2}.\end{aligned} \tag{90}$$

These various derivatives require the knowledge of $\frac{\partial F_L}{\partial U_L}$ and $\frac{\partial F_R}{\partial U_R}$. They correspond to the Jacobian matrix of the Euler equations. Slight changes have to be done with the two-phase flow model. They are detailed in Appendices E and F.

Appendix D. High order extension

MUSCL type reconstruction [57] is considered. Variables extrapolation from the cell centre i and the cell boundary (ij) is achieved by the following relation:

$$f_{ij} = f_i + \Phi_i \overrightarrow{\nabla f}_i \cdot \overrightarrow{r_{ij}} \tag{91}$$

where $\overrightarrow{r_{ij}}$ is the vector connecting the cell centre and the inter-cell face, $\overrightarrow{\nabla f}_i$ is the approximate gradient of variable f in cell i and Φ_i the limiter ($\Phi_i \leqslant 1$).

The gradient is approximated by weighted least squares. From the gradient $\overrightarrow{\nabla f}$ definition,

$$df = \overrightarrow{\nabla f} \cdot \overrightarrow{dM}, \tag{92}$$

with the following notations,

$$\overrightarrow{\nabla f} = \begin{pmatrix} a \\ b \\ c \end{pmatrix},$$

the various gradient components a, b and c, are determined as follows. Relation (92) expressed between the various cell faces and the cell centre provides N relations ($N = 3$ for triangles):

$$f_j - f_i = a(x_j - x_i) + b(y_j - y_i) + c(z_j - z_i), \quad j = 1, N \tag{93}$$

where f_j represents the value of the f function at the centre of the j cell while x_j, y_j and z_j represent the coordinates of the j cell centre.

Thus, the following overdetermined system is obtained:

$$M\Delta f = D \tag{94}$$

where M is an $(N \times 3)$ matrix whereas Δf and D are size 3 vectors. To make benefit of this over-determination, system (94) is multiplied by the M transpose.

$$M^T M \Delta f = M^T D. \tag{95}$$

A new system is thus obtained,

$$M^* \Delta f = D^*. \tag{96}$$

However, the matrix M^* determinant can become very small if some cells are very deformed. To overcome this situation, one way to proceed is to use weights. A very simple weighting procedure has been proposed in [58]. It consists in using the weight $w_{i,j} = \frac{1}{\sqrt{\Delta x_{i,j}^2 + \Delta y_{i,j}^2 + \Delta z_{i,j}^2}}$.

This correction guarantees that the determinant of M^* is $O(1)$.

The last step in the higher order extension method deals with gradients limitation. The Barth and Jespersten [59] method is adopted.

Appendix E. Mixture pressure derivatives

The mixture pressure for the two-phase non-equilibrium model reads:

$$P = \sum_{k=1}^{N} \alpha_k p_k$$

where N is the number of fluids.

With the help of the EOS (4) it becomes:

$$P = \sum_{k=1}^{N} \left[(\gamma_k - 1)\alpha_k \rho_k e_k - \alpha_k \gamma_k P_{\infty,k} \right]. \tag{97}$$

The volume fraction of fluid N is determined from the saturation constraint:

$$\alpha_N = 1 - \sum_{k=1}^{N-1} \alpha_k.$$

Thus, Eq. (97) becomes:

$$P = \sum_{k=1}^{N} (\gamma_k - 1)\alpha_k \rho_k e_k + \sum_{k=1}^{N-1} \alpha_k (\gamma_N P_{\infty,N} - \gamma_k P_{\infty,k}) - \gamma_N P_{\infty,N} \tag{98}$$

with the following derivatives:

$$\frac{\partial P}{\partial \alpha_k \rho_k e_k} = \gamma_k - 1, \qquad \frac{\partial P}{\partial \alpha_k} = (\gamma_N P_{\infty,N} - \gamma_k P_{\infty,k}).$$

Appendix F. Implicit schemes for non-conservative equations of the two-phase flow model

F.1. Volume fraction implicit scheme

In one dimension, the volume fraction equation of system (6) reads:

$$\frac{\partial \alpha_1}{\partial t} + u \frac{\partial \alpha_1}{\partial x} = 0.$$

The Godunov method for advection equations reads:

$$\alpha_{1,i}^{n+1} = \alpha_{1,i}^{n} + \frac{\Delta t}{\Delta x} \left[(\alpha_{1,i-1}^{n} - \alpha_i^n) S^+_{M,i-\frac{1}{2}} - (\alpha_{1,i+1}^{n} - \alpha_i^n) S^-_{M,i+\frac{1}{2}} \right]$$

where S_M represents the contact wave speed and

$$S^+_{M,i-\frac{1}{2}} = \frac{1}{2}\left(1 + sign(S_{M,i-\frac{1}{2}})\right) S_{M,i-\frac{1}{2}}, \qquad S^-_{M,i+\frac{1}{2}} = \frac{1}{2}\left(1 - sign(S_{M,i+\frac{1}{2}})\right) S_{M,i+\frac{1}{2}}.$$

Let's denote,

$$\begin{cases} f^n_{Li} = (\alpha_{1,i-1}^{n} - \alpha_i^n) S^+_{M,i-\frac{1}{2}} = \left(1 + sign(S_{M,i-\frac{1}{2}})\right)(\alpha_{1,i-1}^{n} - \alpha_i^n) \dfrac{S_{M,i-\frac{1}{2}}}{2}, \\ f^n_{Ri} = (\alpha_{1,i+1}^{n} - \alpha_i^n) S^-_{M,i+\frac{1}{2}} = \left(1 - sign(S_{M,i+\frac{1}{2}})\right)(\alpha_{1,i+1}^{n} - \alpha_i^n) \dfrac{S_{M,i+\frac{1}{2}}}{2}. \end{cases}$$

Thus, the implicit scheme for the volume fraction equation reads:

$$\alpha_{1,i}^{n+1} = \alpha_{1,i}^{n} - \frac{\Delta t}{\Delta x} \left[f^{n+1}_{Ri} - f^{n+1}_{Li} \right]. \tag{99}$$

It is worth to mention that $f_{Ri} \neq f_{Li+1}$ as the equation is non-conservative.

Using the same development as previously ((46)–(47)), with $\delta\alpha_i = \alpha_{1,i}^{n+1} - \alpha_{1,i}^{n}$, the following scheme is obtained,

$$-\frac{\Delta t}{\Delta x} \frac{\partial f_{Ri}}{\partial U_{i-1}} \delta\alpha_{i-1} + \left[I + \frac{\Delta t}{\Delta x} \left(\frac{\partial f_{Ri}}{\partial U_i} - \frac{\partial f_{Li}}{\partial U_i} \right) \right] \delta\alpha_i + \frac{\Delta t}{\Delta x} \frac{\partial f_{Ri}}{\partial U_{i+1}} \delta\alpha_{i+1} = -\frac{\Delta t}{\Delta x} \left(f^n_{Ri} - f^n_{Li} \right), \tag{100}$$

where U represents the whole conservative variables vector.

F.2. Internal energies implicit scheme

In one dimension, the internal energy equations read ($k = 1, 2$):

$$\frac{\partial \alpha_k \rho_k e_k}{\partial t} + \frac{\partial \alpha_k \rho_k e_k u}{\partial x} + \alpha_k p_k \frac{\partial u}{\partial x} = 0. \tag{101}$$

The explicit scheme used for this equation reads:

$$(\alpha\rho e)_k^{n+1} = (\alpha\rho e)_k^n - \frac{\Delta t}{\Delta x}\left((\alpha\rho e u)_{k,i+\frac{1}{2}}^{*,n} - (\alpha\rho e u)_{k,i-\frac{1}{2}}^{*,n} + (\alpha p)_{k,i}^n \left(u_{i+\frac{1}{2}}^{*,n} - u_{i-\frac{1}{2}}^{*,n}\right)\right) \tag{102}$$

where the product $(\alpha_k p_k)_i^n$ is assumed constant during the time step and the superscript "*" denotes the Riemann problem solution state.

Thus, the implicit scheme for the internal energy equations read:

$$(\alpha\rho e)_k^{n+1} = (\alpha\rho e)_k^n - \frac{\Delta t}{\Delta x}\left((\alpha\rho e u)_{k,i+\frac{1}{2}}^{*,n+1} - (\alpha\rho e u)_{k,i-\frac{1}{2}}^{*,n+1} + (\alpha p)_{k,i}^{n+1} \left(u_{i+\frac{1}{2}}^{*,n+1} - u_{i-\frac{1}{2}}^{*,n+1}\right)\right). \tag{103}$$

Using the same development as previously ((46)–(47)) with $F_{ek} = (\alpha\rho e u)_k$ and $\delta(\alpha\rho e)_{k,o} = (\alpha\rho e)_{k,i}^{n+1} - (\alpha\rho e)_{k,i}^n$, the following scheme is obtained:

$$\begin{aligned}
&-\frac{\Delta t}{\Delta x}\left[\frac{\partial F_{ek,i-\frac{1}{2}}}{\partial U_{i-1}} + (\alpha p)_{k,i}^n \frac{\partial u_{i-\frac{1}{2}}^*}{\partial U_{i-1}}\right]\delta(\alpha\rho e)_{k,i-1} \\
&\quad + \left[I + \frac{\Delta t}{\Delta x}\left(\frac{\partial F_{ek,i+\frac{1}{2}}^n}{\partial U_i} - \frac{\partial F_{ek,i-\frac{1}{2}}^n}{\partial U_i} + (\alpha p)_{k,i}^n \left[\frac{\partial u_{i+\frac{1}{2}}^*}{\partial U_i} - \frac{\partial u_{i-\frac{1}{2}}^*}{\partial U_i}\right] + \left(u_{i+\frac{1}{2}}^* - u_{i-\frac{1}{2}}^*\right)\frac{\partial (\alpha p)_{k,i}^n}{\partial U_i}\right)\right]\delta(\alpha\rho e)_{k,i} \\
&\quad + \frac{\Delta t}{\Delta x}\left[\frac{\partial F_{ek,i+\frac{1}{2}}}{\partial U_{i+1}} + (\alpha p)_{k,i}^n \frac{\partial u_{i+\frac{1}{2}}^*}{\partial U_{i+1}}\right]\delta(\alpha\rho e)_{k,i+1} \\
&= -\frac{\Delta t}{\Delta x}\left((\alpha\rho e u)_{k,i+\frac{1}{2}}^{*,n} - (\alpha\rho e u)_{k,i-\frac{1}{2}}^{*,n} + (\alpha p)_{k,i}^n \left(u_{i+\frac{1}{2}}^{*,n} - u_{i-\frac{1}{2}}^{*,n}\right)\right)
\end{aligned} \tag{104}$$

where $\frac{\partial F_{ek,i+\frac{1}{2}}}{\partial U_i}$, $\frac{\partial F_{ek,i+\frac{1}{2}}}{\partial U_{i+1}}$, $\frac{\partial F_{ek,i-\frac{1}{2}}}{\partial U_i}$ and $\frac{\partial F_{ek,i-\frac{1}{2}}}{\partial U_{i-1}}$ are calculated using the HLLC flux derivatives (Appendix C).

Appendix G. Stiff thermodynamic relaxation

The following relaxation solver is used to compute the thermodynamic state and in particular the various mass fractions when stiff thermodynamic relaxation is assumed. A two-phase liquid–vapour mixture in thermodynamic equilibrium is considered. Both phases are thus in pressure, temperature and Gibbs free energy equilibrium.

The thermodynamic equilibrium state is determined by considering the following algebraic system:

$$\begin{aligned}
&v = \frac{1}{\rho} = Y_1 v_1 + Y_2 v_2 = cte = v_0, \\
&e = Y_1 e_1 + Y_2 e_2 = cte = e_0, \\
&T_1 = T_2 = T, \\
&p_1 = p_2 = p, \\
&g_1 = g_2
\end{aligned} \tag{105}$$

where $Y_1 = \frac{\alpha_1\rho_1}{\rho}$ and $Y_2 = \frac{\alpha_2\rho_2}{\rho} = 1 - Y_1$ denote the mass fractions of both phases, which are not constant during the relaxation process.

The first two equations of this system come from the mass conservation and mixture total energy conservation, respectively. The last equation represents the Gibbs free energies equality ($g = h - Ts$).

The liquid and its vapour are denoted by the subscripts "1" and "2", respectively.

The specific volumes and the internal energies of each phase are given by the following expressions, based on the stiffened-gas EOS (4):

$$v_k = \frac{(\gamma_k - 1) C_{v,k} T_k}{p_k + p_{\infty,k}}, \tag{106}$$

$$e_k = C_{v,k} T_k \left(1 + \frac{(\gamma_k - 1) p_{\infty,k}}{p + p_{\infty,k}}\right) + q_k. \tag{107}$$

Each parameter involved in the previous expressions $(\gamma_k, C_{v,k}, p_{\infty,k}, q_k)$ is calculated in order to fit the liquid–vapour phase diagram, more precisely the corresponding saturation curves. Details regarding the EOS parameters determination are given in [35] and [2].

Denoting the final state by the superscript '*', the mass conservation constraint becomes:

$$v_0 = Y_1^* v_1^*(p^*) + Y_2^* v_2^*(p^*) = Y_1^* v_1^*(p^*) + (1 - Y_1^*) v_2^*(p^*), \tag{108}$$

with $v_1^*(p^*) = \frac{(\gamma_k - 1) C_{v,k} T^*(p^*)}{p^* + p_{\infty,k}}$.

Constraints of pressures, temperatures and Gibbs free energies equilibrium have been used in relation (108). Indeed, the Gibbs free energies equality leads to a relationship between the pressure and the temperature:

$$T^*(p^*) = T_{sat}(p^*). \tag{109}$$

$v_1^*(p^*)$ and $v_2^*(p^*)$ represent the saturated specific volumes of both phases. A first relation linking the liquid mass fraction and the pressure is thus obtained,

$$Y_1^* = \frac{v_2^*(p^*) - v_0}{v_2^*(p^*) - v_1^*(p^*)}. \tag{110}$$

Consider now the mixture total energy conservation,

$$e_0 = Y_1^* e_1^*(p^*) + Y_2^* e_2^*(p^*) = Y_1^* e_1^*(p^*) + (1 - Y_1^*) e_2^*(p^*) \tag{111}$$

with $e_k(p^*) = C_{v,k} T_k^*(p^*)\left(1 + \frac{(\gamma_k - 1) p_{\infty,k}}{p + p_{\infty,k}}\right) + q_k$.

A second relation linking the liquid mass fraction and the pressure is thus obtained,

$$Y_1^* = \frac{e_0 - e_2^*(p^*)}{e_1^*(p^*) - e_2^*(p^*)}. \tag{112}$$

This relation can be also expressed as a function of the specific enthalpies of the phases,

$$Y_1^* = \frac{h_2^*(p^*) - (e_0 - p^* v_0)}{h_2^*(p^*) - h_1^*(p^*)} \tag{113}$$

where h_1 and h_2 are linked by $h_2^*(p^*) - h_1^*(p^*) = L_v(p^*)$, $L_v(p^*)$ representing the latent heat of vapourization, which is a function of the pressure.

From the previous mass fraction equations, a single function of the pressure is obtained,

$$\frac{h_2^*(p^*) - (e_0 - p^* v_0)}{h_2^*(p^*) - h_1^*(p^*)} - \frac{v_2^*(p^*) - v_0}{v_2^*(p^*) - v_1^*(p^*)} = 0. \tag{114}$$

Its solution is computed with the Newton method. Once the relaxed pressure is determined, the remaining variables are easily computed with the preceding thermodynamic relations.

References

[1] A. Kapila, R. Menikoff, J. Bdzil, S. Son, D. Stewart, Two-phase modeling of deflagration-to-detonation transition in granular materials: Reduced equations, Phys. Fluids 13 (2001) 3002–3024.
[2] R. Saurel, F. Petitpas, R. Abgrall, Modelling phase transition in metastable liquids: Application to cavitating and flashing flows, J. Fluid Mech. 607 (2008) 313–350.
[3] R. Saurel, F. Petitpas, R.A. Berry, Simple and efficient methods relaxation for interfaces separating compressible fluids, cavitating flows and shocks in multiphase mixtures, J. Comput. Phys. 228 (2009) 1678–1712.
[4] C. Hirt, B. Nichols, Volume of fluid (VOF) method for the dynamics of free boundaries, J. Comput. Phys. 3 (1981) 201–255.
[5] B. Lafaurie, C. Nardone, R. Scardovelli, S. Zaleski, G. Zanetti, Modelling merging and fragmentation in multiphase flows with SURFER, J. Comput. Phys. 113 (1994) 134–147.
[6] T. Menard, S. Tanguy, A. Berlemont, Coupling Level Set/VOF/Ghost Fluid methods. Validations and application to 3D simulation of the primary break-up of a liquid jet, Int. J. Multiph. Flow 33 (5) (2007) 510–524.
[7] J. Glimm, J. Grove, X. Li, K. Shyue, Q. Zhang, Y. Zeng, Three dimensional front tracking, SIAM J. Sci. Comput. 19 (1998) 703–727.
[8] R. Fedkiw, T. Aslam, B. Merriman, S. Osher, A non-oscillatory Eulerian approach to interfaces in multimaterial flows (the Ghost Fluid Method), J. Comput. Phys. 152 (2) (1999) 457–492.
[9] R. Abgrall, How to prevent pressure oscillations in multicomponent flow calculations: A quasi conservative approach, J. Comput. Phys. 125 (1996) 150–160.
[10] R. Saurel, R. Abgrall, A multiphase Godunov method for multifluid and multiphase flows, J. Comput. Phys. 150 (1999) 425–467.
[11] D. Juric, G. Tryggvason, Computations of boiling flows, Int. J. Multiph. Flow 24 (3) (1998) 387–410.
[12] A.B. Wood, A Textbook of Sound, G. Bell and Sons Ltd., 1930.
[13] F. Harlow, A. Amsden, A numerical fluid dynamics calculation method for all flow speeds, J. Comput. Phys. 8 (2) (1971) 197–213.
[14] E. Turkel, Preconditioned methods for solving the incompressible and low speed compressible equations, J. Comput. Phys. 72 (2) (1987) 277–298.
[15] V. Ransom, J. Trapp, R. Wagner, Relap/mod3 code manual, NUREG/CR-5535, INEL-95/0174, 1995.

[16] F. Barre, M. Bernard, The Cathare code strategy and assessment, Nucl. Eng. Des. 124 (3) (1990) 257–284.
[17] R.F. Kunz, D.A. Boger, D.R. Stinebring, T.S. Chyczewski, J.W. Lindau, H.J. Gibeling, S. Venkateswaran, T. Govindan, A preconditioned Navier–Stokes method for two-phase flows with application to cavitation prediction, Comput. Fluids 29 (8) (2000) 849–875.
[18] S. Venkateswaran, J.W. Lindau, R.F. Kunz, C.L. Merkle, Computation of multiphase mixture flows with compressibility effects, J. Comput. Phys. 180 (1) (2002) 54–77.
[19] H. Guillard, C. Viozat, On the behaviour of upwind schemes in the low Mach number limit, Comput. Fluids 28 (1999) 63–86.
[20] G. Perigaud, R. Saurel, A compressible flow model with capillary effects, J. Comput. Phys. 209 (2005) 139–178.
[21] S. Kokh, F. Lagoutière, An anti-diffusive numerical scheme for the simulation of interfaces between compressible fluids by means of a five-equation model, J. Comput. Phys. 229 (8) (2010) 2773–2809.
[22] R. Shukla, C. Pantano, J. Freund, An interface capturing method for the simulation of multi-phase compressible flows, J. Comput. Phys. 229 (19) (2010) 7411–7439.
[23] K. So, X. Hu, N. Adams, Anti-diffusion interface sharpening technique for two-phase compressible flow simulations, J. Comput. Phys. 231 (11) (2012) 4304–4323.
[24] R. Saurel, O. Le Métayer, J. Massoni, S. Gavrilyuk, Shock jump relations for multiphase mixtures with stiff mechanical relaxation, Shock Waves 16 (2007) 209–232.
[25] F. Petitpas, E. Franquet, R. Saurel, O. Le Metayer, A relaxation-projection method for compressible flows. Part II: Artificial heat exchanges for multiphase shocks, J. Comput. Phys. 225 (2) (2007) 2214–2248.
[26] F. Petitpas, R. Saurel, E. Franquet, A. Chinnayya, Modelling detonation waves in condensed energetic materials: Multiphase CJ conditions and multidimensional computations, Shock Waves 19 (2009) 377–401.
[27] S. Schoch, N. Nikiforakis, B.J. Lee, R. Saurel, Multi-phase simulation of ammonium nitrate emulsion detonations, Combust. Flame 160 (9) (2013) 1883–1899.
[28] Y. Choi, C. Merkle, The application of preconditioning in viscous flows, J. Comput. Phys. 105 (2) (1993) 207–223.
[29] D.G. Ebin, The motion of slightly compressible fluids viewed as a motion with strong constraining force, Ann. Math. 105 (1) (1977) 141–200.
[30] S. Klainerman, A. Majda, Singular limits of quasilinear hyperbolic systems with large parameters and the incompressible limit of compressible fluids, Commun. Pure Appl. Math. 34 (4) (1981) 481–524.
[31] S. Schochet, The compressible Euler equations in a bounded domain: Existence of solutions and the incompressible limit, Commun. Math. Phys. 104 (1) (1986) 49–75.
[32] G. Metivier, S. Schochet, The incompressible limit of the non-isentropic Euler equations, Arch. Ration. Mech. Anal. 158 (1) (2001) 61–90.
[33] T. Alazard, Low Mach number limit of the full Navier–Stokes equations, Arch. Ration. Mech. Anal. 180 (1) (2006) 1–73.
[34] E. Toro, M. Spruce, W. Speares, Restoration of the contact surface in the HLL-Riemann solver, Shock Waves 4 (1994) 25–34.
[35] O. Le Métayer, J. Massoni, R. Saurel, Élaboration des lois d'état d'un liquide et de sa vapeur pour les modèles d'écoulements diphasiques, Int. J. Therm. Sci. 43 (3) (2004) 265–276 (in French).
[36] D. Babii, S.K. Godunov, V. Zhukov, O. Feodoritova, On the different approximations of overdetermined hyperbolic equations of classical mathematical physics, Comput. Math. Math. Phys. 47 (3) (2007) 427–441.
[37] F. Petitpas, J. Massoni, R. Saurel, E. Lapebie, L. Munier, Diffuse interface model for high speed cavitating underwater systems, Int. J. Multiph. Flow 35 (8) (2009) 747–759.
[38] R. Saurel, N. Favrie, F. Petitpas, M.-H. Lallemand, S. Gavrilyuk, Modelling dynamic and irreversible powder compaction, J. Fluid Mech. 664 (2010) 348–396.
[39] N. Favrie, S. Gavrilyuk, R. Saurel, Solid–fluid diffuse interface model in cases of extreme deformations, J. Comput. Phys. 228 (16) (2009) 6037–6077.
[40] R.A. Berry, R. Saurel, O. LeMetayer, The discrete equation method (dem) for fully compressible, two-phase flows in ducts of spatially varying cross-section, Nucl. Eng. Des. 240 (11) (2010) 3797–3818.
[41] S. Osher, S. Chakravarthy, Upwind schemes and boundary conditions with applications to Euler equations in general geometries, J. Comput. Phys. 50 (3) (1983) 447–481.
[42] E. Turkel, N. Vatsa, Local preconditioners for steady and unsteady flow applications, ESAIM: Math. Model. Numer. Anal. 39 (2005) 515–535.
[43] P. Birken, G. Gassner, M. Haas, C. Munz, Preconditioning for modal discontinuous Galerkin methods for unsteady 3d Navier–Stokes equations, J. Comput. Phys. 240 (0) (2013) 20–35.
[44] R. Fortes-Patella, O. Coutier-Delgosha, J. Reboud, Evaluation of the turbulence model influence on the numerical simulations of unsteady cavitation, J. Fluids Eng. 125 (1) (2003) 38–45.
[45] A. Murrone, H. Guillard, Behavior of upwind scheme in the low Mach number limit: III. Preconditioned dissipation for a five equation two phase model, Comput. Fluids 37 (10) (2005) 1209–1224.
[46] B. Braconnier, B. Nkonga, An all-speed relaxation scheme for interface flows with surface tension, J. Comput. Phys. 228 (16) (2009) 5722–5739.
[47] P. Wegener, Nonequilibrium Flow, Marcel Dekker, New York, 1969.
[48] P. Birken, A. Meister, On low Mach number preconditioning of finite volume schemes, Proc. Appl. Math. Mech. 5 (2005) 759–760.
[49] S. Balay, J. Brown, K. Buschelman, W.D. Gropp, D. Kaushik, M.G. Knepley, L.C. McInnes, B.F. Smith, H. Zhang, PETSc Web page, http://www.mcs.anl.gov/petsc, 2013.
[50] S. Balay, J. Brown, K. Buschelman, V. Eijkhout, W.D. Gropp, D. Kaushik, M.G. Knepley, L.C. McInnes, B.F. Smith, H. Zhang, PETSc users manual, Tech. Rep. ANL-95/11 – Revision 3.4, Argonne National Laboratory, 2013.
[51] S. Balay, W.D. Gropp, L.C. McInnes, B.F. Smith, Efficient management of parallelism in object oriented numerical software libraries, in: E. Arge, A.M. Bruaset, H.P. Langtangen (Eds.), Modern Software Tools in Scientific Computing, Birkhäuser, 1997, pp. 163–202.
[52] H. Guillard, On the behavior of upwind schemes in the low Mach number limit. IV: P0 approximation on triangular and tetrahedral cells, Comput. Fluids 38 (10) (2009) 1969–1972.
[53] S. Dellacherie, P. Omnes, F. Rieper, The influence of cell geometry on the Godunov scheme applied to the linear wave equation, J. Comput. Phys. 229 (14) (2010) 5315–5338.
[54] Y. Saad, Numerical Methods for Large Eigenvalue Problems, Manchester University Press, 1992.
[55] S. Davis, Simplified second-order Godunov-type methods, SIAM J. Sci. Stat. Comput. 9 (1988) 445–473.
[56] A. Harten, P. Lax, B. van Leer, On upstream differencing and Godunov-type schemes for hyperbolic conservation laws, SIAM Rev. 25 (1983) 35–61.
[57] B. Van Leer, Towards the ultimate conservative difference scheme. V. A second order sequel to Godunov's method, J. Comput. Phys. 32 (1979) 445–473.
[58] D. Mavripilis, Revisiting the least-squares procedure for gradient reconstruction on unstructured meshes, in: AIAA 16th Computational Fluid Dynamics Conference, 2003, p. 3986.
[59] T. Barth, D. Jespersten, The design and application of upwind schemes on unstructured meshes, in: Proceedings of the AIAA 27th Aerospace Sciences Meeting, Reno, Nevada, 1989.